

The Compressive Behavior of Glass Fiber Reinforced Composites Subjected to Local Thermal Loading

by

Catherine Meaghan Westover

B.S. (United States Naval Academy) 1998

A thesis submitted in partial satisfaction of the requirements for the degree of

Master of Engineering  
in

Engineering-Mechanical Engineering

in the

GRADUATE DIVISION

of the

UNIVERSITY OF CALIFORNIA, BERKELEY

Committee in charge:

Professor C.K.H. Dharan, Chair

Professor C. Fernandez-Pello

Professor P.J. Pagni

**DISTRIBUTION STATEMENT A**


Approved for Public Release


Distribution Unlimited

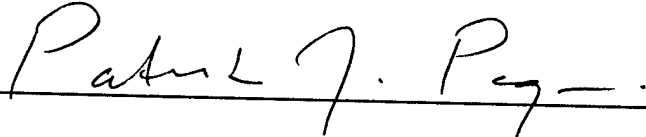
Spring 2000

20010323 066

The thesis of Catherine Meaghan Westover is approved:

 4-25-2000  
Chair Date

 5/3/00  
Date

 5/15/2000  
Date

University of California, Berkeley

Spring 2000

## Abstract

### The Compressive Behavior of Glass Fiber Composites Subjected to Local Thermal Loading

by

Catherine Meaghan Westover

Master of Engineering in Mechanical Engineering

University of California, Berkeley

Professor C.K.H. Dharan, Chair

An experimental study has been conducted to determine the effects of local thermal loading on the compressive behavior of glass fiber composites. The primary factors considered were the intensity of thermal loading and the applied compressive load. The material specimens tested were laminate plates composed of Micarta G10 FR4, a fire retardant glass/epoxy laminate. Two types of testing were conducted for heat fluxes of  $85 \text{ kW/m}^2$ ,  $140 \text{ kW/m}^2$ , and  $195 \text{ kW/m}^2$ . The first type involved the unloaded radiant thermal testing of the material and provided a baseline from which the effects of thermal loading on the physical properties of the composite specimen were determined. The second type was a combined loading test, which involved loading specimens in compression to a constant applied load and subjecting them to a local thermal load.

From the radiant thermal tests, the primary physical damage observed was delamination and charring. In the combined loading tests, delamination and charring were again present, however, microbuckling was the primary form of damage leading to catastrophic failure. An evaluation determined delamination and charring damage to be

dependent upon the thermal load while the existence of microbuckling proved dependent upon both the thermal load and the applied compressive load. Microbuckling was extensively investigated and determined to be a function of the degradation of the material's fiber microbuckling strength. From the results, design limitations were developed to minimize the potential effects of local thermal loading. These limitations included optimizing the thickness of the composite structure and minimizing the applied compressive load. Maximizing the thickness results in increased buckling strengths and load carrying capacities, while decreasing the concentration of thermal energy and the degree of damage. Minimizing the applied compressive load reduces the chance of microbuckling and global buckling, thereby, decreasing the chance of catastrophic failure in the case of thermal loading. A post-exposure evaluation can also be developed from the results presented.

## **Dedication**

I would like to dedicate this work to the following people.

To my friends; through our relationships, I have learned the many lessons of diversity, culture and friendship that made my experiences at Berkeley invaluable. To my family, who consistently battles my doubt with encouragement and support. You have loved me unconditionally and have provided me with the support and guidance to accomplish my goals. And to Tim, who despite a separation of 2000 miles and two time zones, was with me through it all. Your love, understanding, and humor these past two years is irreplaceable.

## **Acknowledgements**

I would first like to acknowledge the U.S. Navy for giving me the opportunity and support to pursue a Master of Engineering degree. Their assistance made it possible to attend this institution and to attain an academic experience that will benefit me greatly as an officer in their fleet and beyond. I also thank Carla Trujillo, whose confidence and guidance brought me to Berkeley initially and inspired me throughout.

Many thanks to Professor Dharan, who provided me with the inspiration, advice and support to pursue this research. Thanks also to the Berkeley Composites Laboratory. The time and effort they provided in the area of materials testing and analysis is greatly appreciated. I am also grateful for the assistance of YLA Plastics who conducted dynamic mechanical analysis testing in support of this research.

Many thanks to Professor Fernandez-Pello and his lab for the opportunity and support to work in the Microgravity Combustion Lab. The knowledge and assistance that they provided in the field of combustion enabled me to accomplish my research goals, as well as, instilled a new enthusiasm for combustion!

## Table of Contents

<b>Dedication .....</b>	<b>i</b>
<b>Acknowledgements .....</b>	<b>ii</b>
<b>Table of Contents.....</b>	<b>iii</b>
<b>List of Figures .....</b>	<b>v</b>
<b>List of Tables.....</b>	<b>vii</b>
<b>Chapter 1. Introduction .....</b>	<b>1</b>
1.1 Motivation .....	1
1.1.1 Naval Applications of Glass Reinforced Polymer Matrix Composites.....	1
1.1.2 Thermal Loading Limitations .....	2
1.2 Background and Literature Review .....	4
1.2.1 Compressive Behavior of Composite Laminates.....	4
1.2.2 Mechanical Response of Composite Laminates to Thermal Loading.....	6
1.2.3 Literature Review.....	7
1.3 Current Research.....	15
<b>Chapter 2. Experimental Equipment .....</b>	<b>17</b>
2.1 Material Specimens.....	17
2.2 Mechanical Testing Apparatus .....	19
2.2.1 Compression Testing Fixture.....	19
2.2.2 Instrumentation and Test Machine.....	20
2.3 Thermal Hardware .....	21
2.3.1 Infrared Radiant Spot Heater .....	21
2.3.2 Radiometer Calibration .....	22
2.3.3 Infrared Camera .....	23
2.4 Safety Precautions.....	24
<b>Chapter 3. Experimental Results .....</b>	<b>26</b>
3.1 Introduction .....	26
3.2 Testing Parameters.....	27
3.2.1 Specimen Geometry .....	27
3.2.2 Applied Compressive Load .....	27
3.2.3 Applied Thermal Load .....	28
3.2.4 Test Duration .....	29
3.3 Unloaded Thermal Tests .....	31
3.3.1 Method.....	31
3.3.2 Infrared Images .....	32
3.3.3 Material Damage.....	35
3.4 Combined Loading Tests .....	38
3.4.1 Method.....	38
3.4.2 Combined Loading Test Results.....	41
<b>Chapter 4. Theoretical Analysis and Discussion .....</b>	<b>46</b>
4.1 Introduction .....	46
4.2 Background .....	47
4.3 Modulus Measurements and Evaluation.....	51
4.3.1 Modulus Measurement through DMA .....	51

4.3.2	Evaluation of Experimental Results.....	52
4.4	Evaluation of Damage.....	55
4.4.1	Delamination.....	55
4.4.2	Microbuckling Analysis .....	55
4.4.3	Discussion.....	61
<b>Chapter 5.</b>	<b>Summary and Conclusions .....</b>	<b>65</b>
<b>References</b>	<b>.....</b>	<b>69</b>
<b>Appendix A</b>	<b>Compression Test Fixture .....</b>	<b>71</b>
<b>Appendix B</b>	<b>Theoretical Euler Buckling Analysis.....</b>	<b>74</b>
<b>Appendix C</b>	<b>Specimen Damage Measurements .....</b>	<b>75</b>
<b>Appendix D</b>	<b>Stress Concentration Analysis.....</b>	<b>76</b>
<b>Appendix E</b>	<b>DMA Analysis .....</b>	<b>81</b>

## List of Figures

Figure 1.1	Buckling delamination .....	5
Figure 1.2	Fiber microbuckling.....	5
Figure 1.3	Asaro and Dao collapse model .....	11
Figure 1.4	Critical collapse load versus center temperature $T_c$ for (a)case #1 and (b) case #.....	13
Figure 2.1	Compression test fixture.....	19
Figure 2.2	Concentrated thermal energy produced by the infrared heater.....	22
Figure 2.3	Infrared spot heater calibration at a distance 25.0 mm from the heater collar .....	23
Figure 2.4	Portable ventilation system: (a) hood with plastic isolation curtains and (b) vaccum pump system for filtering combustio products.....	25
Figure 3.1	Thermal images showing stabilization of temperature distribution from (a) four minutes of exposure to (b) five minutes of exposure at $140 \text{ kW/m}^2$ .....	30
Figure 3.2	Solitary thermal loading schematic.....	32
Figure 3.3	Temperature distribution of the specimens at five minutes of exposure for thermal intensities of (a) $85 \text{ kW/m}^2$ , (b) $140 \text{ kW/m}^2$ , and (c) $195 \text{ kW/m}^2$ .....	34
Figure 3.4	Temperature distribution at the specimen midplane after five minutes of thermal loading at specified heat fluxes. Temperature plateaus at $320 \text{ C}$ are due to the range limitations of the thermal imaging equipiment. ....	35
Figure 3.5....	Damage of exposed and unexposed specimen surfaces due to solitary thermal loading at surface. The dark plumes of soot are due to the vertical entrainment of smoke by the hood exhaust system. ....	37
Figure 3.6	Placement of test specimen in the compression testing fixtures: (a) the alignment of the test specimen in the bottom fixture and (b) the alignment of the top fixture with the specimen edge, prior to insertion of the specimen into the top fixture.....	40
Figure 3.7	Alignment of spot heater with test specimen: (a) positioning of the heater on load machine baseplate and (b) energy concentration centered on the test specimen.....	40
Figure 3.8	Ventilation system with curtains and fume ducting.....	41
Figure 3.9	Schematic of failure modes observed .....	42
Figure 3.10	Delamination and charring regions of specimens subjected to a compressive load of $22.1 \text{ MPA}$ and heat fluxes of (a) $85 \text{ kW/m}^2$ , (b) $140 \text{ kW/m}^2$ , and (c) $195 \text{ kW/m}^2$ . The dark plumes of soot are due to the vertical entrainment of smoke by the hood exhaust system .....	44
Figure 3.11	Delamination and charring regions of specimens subjected to a constant heat flux of $85 \text{ kW/m}^2$ and a compressive load of (a) $16.5 \text{ MPa}$ , (b) $19.3 \text{ MPa}$ , and (c) $22.1 \text{ Mpa}$ . The dark plumes of soot are due to the vertical entrainment of smoke by the hood exhaust system.....	44
Figure 3.12	Progression of microbuckling damage with increasing applied compressive loads for a constant thermal loading of $140 \text{ kW/m}^2$ : (a) $8.27 \text{ MPa}$ , (b) $22.1 \text{ MPa}$ , (c) $30.3 \text{ MPa}$ , (d) $30.5 \text{ Mpa}$ . The dark plumes of soot are due to the vertical entrainment of smoke by the hood exhaust system .....	45
Figure 4.1	Shear modulus as a function of temperature for Micarta G10 FR4.....	52

Figure 4.2	The shear modulus of the material and the distance from the mid point of incident heat flux as a function of temperature for heat fluxes of 85 kW/m <sup>2</sup> , 140 kW/m <sup>2</sup> , and 195 kW/m <sup>2</sup> .	53
Figure 4.3	Shear modulus as a function of distance from the mid point of incident heat flux for heat fluxes of 85 kW/m <sup>2</sup> , 140 kW/m <sup>2</sup> , and 195 kW/m <sup>2</sup> .	54
Figure 4.4	Microbuckling ratio, mf/w, versus applied compressive stress for various thermal loading conditions	56
Figure 4.5a	Microbuckling length as a function of applied compressive stress for a thermal load of 85 kW/m <sup>2</sup>	58
Figure 4.5b	Microbuckling length as a function of applied compressive stress for a thermal load of 140 kW/m <sup>2</sup>	59
Figure 4.5c	Microbuckling length as a function of applied compressive stress for a thermal load of 195 kW/m <sup>2</sup>	60
Figure 4.6	Damage ratio as a function of applied compressive stress	63
Figure A.1	Base plate fixture	71
Figure A.2	Bottom fixture	72
Figure A.3	Top fixture	73
Figure D.1	Stress concentration ratio as a function of distance ahead of the hole for a circular hole in an infinite isotropic plate	77
Figure D.2	Normal stress as a function of distance ahead of the hole for a circular hole in an infinite isotropic plate	78
Figure E.1	Micarta G10 Rheometric Temperature Scan	84

## **List of Tables**

Table 2.1	Mechanical properties of Micarta G10 FR4 .....	17
Table 3.1	Buckling properties of Micarta G10 FR4.....	28
Table 3.2a	Thermal damage of exposed surface.....	37
Table 3.2b	Thermal damage of unexposed surface .....	37
Table 4.1	Damage comparison from solitary thermal loading and combined Loading tests.....	56
Table c.1	Specimen Damage Measurements .....	75

## ***Chapter 1 Introduction***

### **1.1 Motivation**

#### **1.1.1 Naval Applications of Glass Reinforced Polymer Matrix Composites**

The use of fiber reinforced polymer matrix composites is beginning to permeate the industry of naval shipbuilding, although, with the exception of the MHC-51 class minesweeper, the Navy had previously rejected the use of these composites in its ship and submarine construction [1]. Due to the increased performance demands of naval vessels, the composite designs that have dominated the recreational maritime industry had been considered inadequate for naval applications. High construction costs and high failure risk due to lack of technical information further kept the Navy from implementing composite materials into their ship and submarine construction. However, as fabrication techniques improve and the need increases for reduced electronic signatures, these materials are becoming more desirable and feasible to the demands of naval shipbuilding [1].

The Navy has traditionally used steel and aluminum for their construction materials. These materials will slowly be replaced with polymer matrix composites that offer improved characteristics and properties. The high strength-to-weight ratio of composites may provide weight saving alternatives in a number of applications including hulls, engine mounts, superstructures, weapon systems, and missile launch tubes. These weight reductions would result in fuel savings and greater cargo capacity as well as increased vessel stability due to decreased top-side weight. In submarines, they may potentially increase depth and balance capabilities [2].

Polymer-matrix composites are non-corrosive, non-metallic materials, which means greater longevity and decreased maintenance than traditional materials exposed to the salt-water environment. Consequently, overall life cycle costs would be reduced from the decreased cleaning, inspection, coating and lubrication requirements of these materials [2].

The use of these materials also results in improved low radar cross-section characteristics that are critical to the operational demands of naval vessels. The most recent minesweeping platform, the MHC-51 class, was constructed of non-magnetic glass reinforced plastics. These materials reduced the ship's vulnerability to magnetic mines as well as increased its protection to ballistic impact due to the increased energy absorption capability of the material relative to its density [3].

#### **1.1.2 Thermal Loading Limitations**

While there is increasing demand for polymer-matrix composites in naval applications, the implementation of composites is limited by their structural susceptibility to fire. Fire is a constant potential hazard and a ship's ability to resist thermal and structural damage is critical to mission accomplishment and personnel safety. The watertight integrity, stability and offensive power of the vessel are dependent on the ability to control damage and maintain structural integrity [4].

With these factors in mind, current standards have been defined by the International Maritime Organization through the International Convention for the Safety of Life at Sea (SOLAS). The standards require hulls, structures, bulkheads, decks and deckhouses to be constructed out of steel or an "equivalent" material, where an "equivalent" material is any non-combustible material which has the structural integrity

equivalent to that of steel at the end of a fire test [2,5]. Currently, there are no design and evaluation criteria that adequately assess the compliance of composite materials to these standards. Although research is being pursued [5,6,7,8], further analyses of the structural failure and resulting structural integrity of composite materials at elevated temperatures need to be evaluated to insure safe and reliable design criteria. Of particular importance is the damage tolerance of composites to fire and the ability of composite structures to withstand fire threats without collapsing and propagating damage to other locations. Due to the critical dependence of composite compressive behavior on temperature, the problem of compressive strength of a composite plate combined with localized thermal heating due to an adjacent fire is addressed in this research.

In the following sections, the compressive behavior of composite laminates is reviewed followed by a description of previous research conducted in the subject area and an outline of the objectives of this research.

## 1.2 Background and Literature Review

### 1.2.1 Compressive Behavior of Composite Laminates

Structural continuous-fiber reinforced polymer matrix composite laminates are usually of orthotropic constructions that lead to unique failure mechanisms in compression. Fracture of these laminates seldom occurs catastrophically and tends to be progressive in nature with subcritical damage widely dispersed throughout the material [9]. Failure mechanisms depend on the laminate geometry and matrix properties and may involve global and/or local failure modes

A thin-walled laminate plate loaded axially in compression may globally experience Euler buckling. Euler buckling occurs when a thin-walled column is subjected to excess axial compressive loads resulting in lateral deflection of the column. The critical load to create buckling is dependent on the bending stiffness ( $EI$ ), the length, and the type of support at the ends of the column. It is defined as

$$P_{CR} = \frac{\pi^2 (EI)}{L_e^2} \quad (1.1)$$

where

$$L_e = KL \quad (1.2)$$

$K$  is the coefficient which describes the end support conditions of the column and it is computed theoretically or empirically to fit experimental data.  $L$  is the actual length of the column [10].

Buckling delamination (Figure 1.1) is another form of global failure that may result from axial compressive loading. Buckling delamination is commonly a result of impact damage, which introduces local microcracks and delamination. This form of

delamination induces Mode 1 loading which causes the delamination to propagate at sufficiently high loads [9].

Local failure may occur in the form of fiber microbuckling (Figure 1.2), the individual buckling of the fibers in the matrix [9]. While high modulus fibers provide excellent strength and stiffness properties in tension, they are unstable in compression. They respond like slender columns experiencing Euler buckling, with increased support provided by the matrix material. Although fiber buckling is a local phenomenon, it can propagate and form kink bands. Microbuckling and kink band formation can lead to global buckling and delamination of the composite laminate plate.

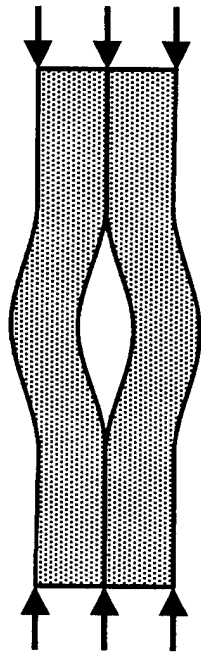


**Figure 1.1 Buckling delamination\***

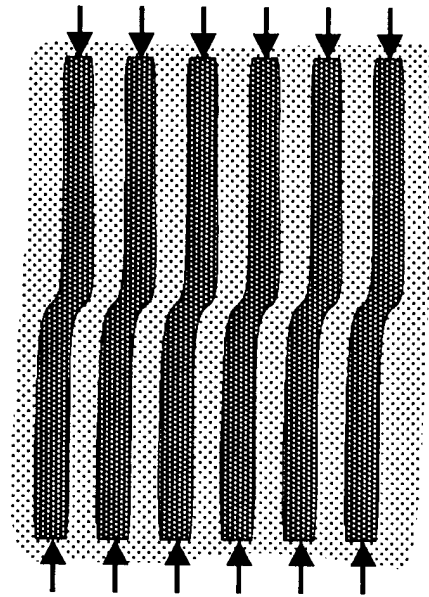


**Figure 1.2 Fiber microbuckling\***

\* Figures adapted from Ref [9].

### **1.2.2 Mechanical Response of Composite Laminates to Thermal Loading**

Due to their anisotropic and inhomogeneous structure, the response of composite laminates to high temperature exposure is more complex than for metallic materials. The stress and failure analyses of these materials under compressive loads at elevated temperatures are dependent upon the elastic modulus. At elevated temperatures, polymer matrix composites typically experience significant degradation of the composite matrix resulting in reduced transverse and interlaminar shear strengths and moduli. The longitudinal compressive strength of PMC laminates is dependent upon these properties. Therefore, as matrix properties rapidly decrease with increasing temperature, there is a loss of fiber confinement and interlaminar shear strength and a reduction in the laminate compressive strength [5].

Polymer matrix composites also have much lower thermal conductivities than metals and metallic alloys, which create larger temperature gradients in the material. These temperature gradients create thermal stresses and degrade material properties resulting in heterogeneous damage modes such as kinking, or microbuckling, and delamination. The type and severity of failure is dependent on the degree and distribution of thermal degradation [11].

At high intensities of thermal loading by means of radiation, conduction, or convection, the material may experience pyrolysis and the subsequent removal of material due to thermal chemical or thermal mechanical ablation. The structural response of PMC laminates near or above the ablation temperature are difficult to predict. These limitations are due to the lack of thermophysical and thermal mechanical properties above these temperatures, the nonlinearity introduced by temperature dependent material

properties and by moving boundary conditions, and the difficulty in assessing the failure mode. The following section includes a description of previous work conducted to investigate the physical response of composite materials to elevated temperatures and briefly summarizes their findings and the applications to this research.

### **1.2.3 Background**

Milke and Vizzini, reference [6], characterized heat transfer through composite laminates using three-dimensional heat transfer analysis. Where previous research had concentrated on two-dimensional analysis, their objective was to incorporate a through-thickness temperature gradient to predict thermally induced stresses in a composite exposed to short-term radiant heating. This type of analysis was necessitated by the transient nature of heat transfer processes associated with short-term fire exposure.

A three-dimensional model was developed to predict both in-plane and through-thickness temperature distributions. The model accounted for the anisotropic properties of composite materials, considering both the longitudinal and transverse conductivity of the fibers as well as the in-plane rotation of the laminate plies. The heating of a thin laminate plate was examined, incorporating the parameters of the ply number, thickness, length, width, initial temperature and thermophysical properties.

Experiments were conducted to demonstrate the accuracy of the thermal response model. Using radiant panels, material specimens were subjected to moderate heat fluxes ranging from 9.1 to 17.6 kW/m<sup>2</sup>. This thermal loading was applied uniformly across the width of the specimen and the unexposed surface temperature of the specimen was measured using an infrared camera system.

This research resulted in an accurate modeling analysis which is applicable to a wide range of sample geometries and material compositions, and which focuses on moderate intensity, short-term thermal exposure. This work, however, did not characterize the effects of high-intensity, short-term thermal loading nor the associated degradation due to pyrolysis, ignition, and ablation or melting. A detailed assessment of mechanical property degradation as a function of the temperature distribution was neglected as well.

Chang [7] also developed a thermal analysis to compute transient temperature distributions. His objective was to determine these temperature distributions as well as the moving boundary conditions that result from material removal, such as ablation and melting. The results from this thermal analysis were then used as input to assess structural performance and integrity.

The thermal modeling approach used by Chang considered the heat transfer analysis at a macroscopic modeling level. The reactions were accounted for by macroscopic modeling parameters such as heat capacity and sublimation energy. The problem was approached as a one-dimensional problem, rather than a three-dimensional problem, and modeled a composite laminate of thickness  $L$  subjected to a uniform constant intensity heat flux on one surface. The bulk thermal response of the slab was computed from conductivities approximated by vectorially integrating the conductivity matrix through the composite thickness.

The mechanical modeling approach involved the development of a finite element code that incorporated the Mindlin laminated plate theory to evaluate structural integrity. This model incorporated the nonlinearity of the material properties due to thermal

degradation and also accounted for the moving boundary conditions caused by thermal ablation and ply failure. Stresses and displacements were evaluated for each ply and then compared with the failure criteria of the composite laminate. Upon ply failure, structural stiffnesses were modified and the stress redistributions were computed. Structural failure of the laminate was defined as the condition when the integrated load carrying capability of the remaining plies was less than the externally applied load.

The analyses were verified through experimental tests in which a mechanical load was applied axially along the plate and intense thermal radiation was applied transversely to the plate. Tests were conducted applying both tensile and compressive loads. The results established reasonably good agreement between the analytical and experimental methods.

Chang's work presents both a thermal and thermal mechanical analysis methodology. It addresses the response of structural integrity to thermally degraded material properties, including the effects of high intensity thermal ablation. It also models a localized thermal loading scenario rather than a uniform thermal loading across the material thickness. However, while it does define a structural failure condition, it does not address modes of failure created by the combined loading conditions or the catastrophic failure mode experienced by the material.

Asaro and Dao [5,8] have conducted detailed investigations of composite failure modes due to thermal and mechanical loading. Their research has been concerned with the thermal degradation of composite materials in marine applications. This work focused on developing a quantitative framework for assessing the degradation of composite material properties under thermal loading. The subsequent degradation of structural

integrity of composite structures can be evaluated through these assessments. Their objective aimed to determine a quantitative description of structural collapse in order to develop a design methodology.

The analysis and experimentation focused on the combined in-plane compressive and out-of-plane mechanical loading of composite plates while exposed to thermal loading. The material specimens tested consisted of E-glass fabric, vacuum infused with a vinylester matrix and thermally insulated with mineral wool on the exposed side. In-plane compressive loading was determined to be critical due to the dependence of fiber confinement and interlaminar shear strength on resin properties, which decrease with increased temperatures. The thermal loading was applied uniformly across the width of the exposed side of the specimen, with significant temperature gradients through the specimen thickness.

The quantitative methodology developed by Dao and Asaro was developed through a combination of experimental and theoretical evaluations. A simple model, shown in Figure 1.3, was used to determine the material property variations and to describe the macroscopic “buckling” collapse modes

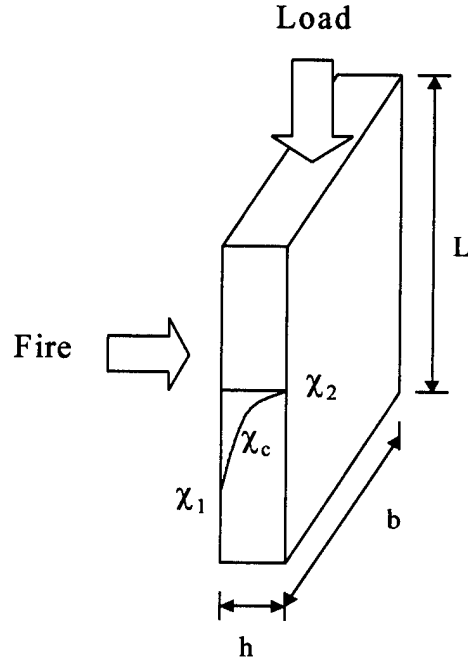


**Figure 1.3 Asaro and Dao collapse model with material property variation [5].**

The plate is assumed to have simply supported end conditions and is subjected to symmetrically applied compressive loads.

This model incorporated temperature dependent stiffness and strength properties. A gradient in material properties was assumed to correspond to the temperature gradient and resulting loss in material stiffness. This property gradient was assumed to be of the form

$$\chi = Ax^2 + Bx + C \quad (1.3)$$

where  $A$ ,  $B$  and  $C$  are defined as follows

$$A = (2\Delta - 4\Delta_1) / h^2, \quad B = (4\Delta_1 - \Delta) / h, \quad C = E_1$$

$$\Delta_1 = E_c - E_1, \quad \Delta = E_2 - E_1. \quad (1.4)$$

$E_1$  represents the “exposed face” property (e.g. modulus),  $E_2$  represents the “back face” or “unexposed face” property, and  $E_c$  is a property value at the panels center.

Asaro and Dao derived the structural integrity from the modulus properties through a simple beam theory analysis, which shows that

$$\frac{P_{coll}}{P_E} = 1 - \frac{1}{12} \Gamma^2 + \frac{2}{15} \Gamma^- \quad (1.5)$$

with

$$\Gamma = \frac{E_2 - E_1}{E_o}, \quad \Gamma^- = \frac{E_2 - 2E_c + E_1}{E_o}, \quad E_o = \frac{E_2 + 4E_c + E_1}{6} \quad (1.6)$$

and  $P_E$  is the Euler buckling load described previously for a rectangular cross-section.

This simplified model was verified through three-dimensional finite element analysis. A finite difference based thermal analysis was conducted to determine the temperature distribution. Using this temperature distribution, a property degradation profile was then determined. From the degraded property profiles and the use of the simplified collapse model, a critical load vs. time profile was calculated which correlated closely to the experimental results.

From their experimental and analytical analysis, Asaro and Dao identified a ‘danger zone’ to determine the structural perseverance of composite materials exposed to fire damage [8]. By fixing the face temperature-time histories at the front face of the panel and choosing two extreme boundary conditions, (1) the insulated back face and (2) the back face at room temperature,  $P_{coll}$  was plotted against the center temperature for two separate cases. Using Figure 1.4, it was predicted that materials loaded above the danger zone would not survive fire damage; materials loaded below the danger zone

would retain structural integrity; and finally, the integrity of any specimens loaded in between would depend on the actual thermal boundary conditions.

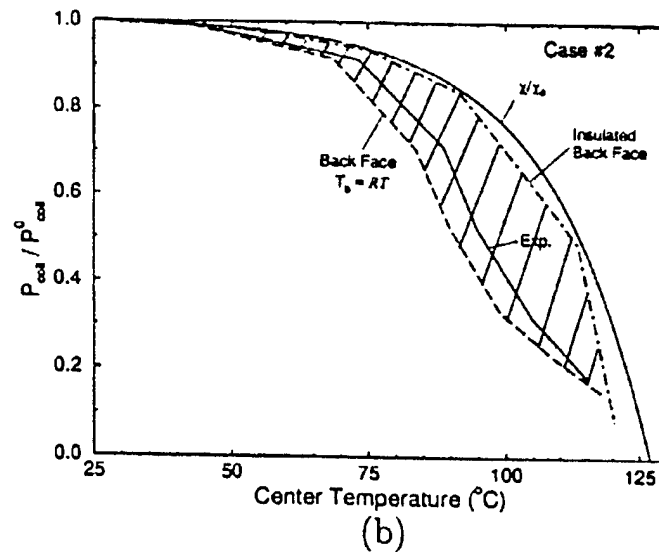
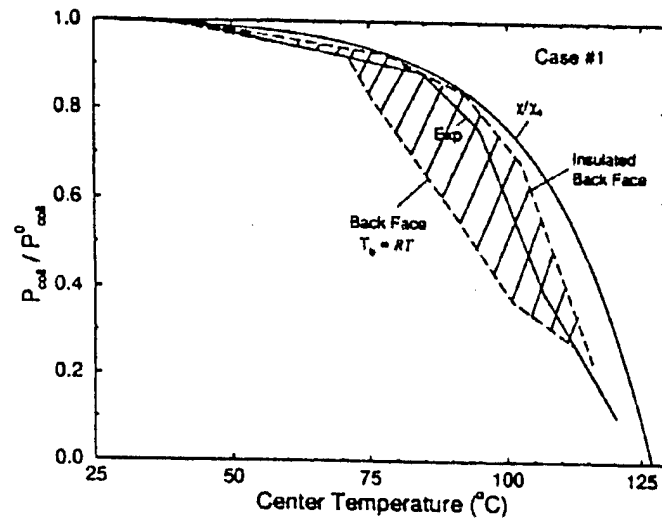


**Figure 1.4 Critical collapse load vs. center temperature  $T_c$  for (a) Case #1 and (b) Case #2 [8].**

Their experimental results showed that, for uniform thermal loading, the dominant failure mode was due to global buckling, and secondary failure modes of kink band formation

and microbuckling were initiated either by embedded thermocouples or overall global buckling. Their work provides a preliminary assessment of structural failure and an evaluation of the structural integrity of composite laminates subjected to thermal loading.

### **1.3 Current Research**

The objective of the present research is to determine the compressive behavior of glass fiber reinforced composites subjected to local thermal loading. Previous research has focused on the heat transfer characteristics of composite laminates and the effects of uniform thermal loading on laminate compressive behavior. However, a study of the compressive strength of laminates subjected to localized thermal loading has not been conducted. The subject of local thermal loading is important due to the gradients in material properties that are created both in-plane and through the thickness of the structure when exposed to local rather than uniform loading conditions. Localized thermal loading is also a more probable scenario in an actual fire such as a compartment fire where damage will occur locally to adjacent structures.

Local thermal loading occurs when the test specimen is subjected to a constant intensity thermal load within a localized region on the specimen's exposed face. This type of loading results in through-thickness and in-plane temperature gradients in the laminate. These temperature gradients create gradients in mechanical properties and unique stress distributions in the material. As a result of these loading conditions, these laminates experience atypical failure modes. The goal of this research is to characterize the mechanisms of failure associated with local thermal loading in order to develop design criteria and an analysis of structural integrity.

Experimental tests were conducted using test specimens of Micarta G10 FR4, a woven E-glass fabric impregnated in a fire retardant matrix. A constant compressive load was applied to the specimen using a screw-driven testing machine. Localized thermal loading was then applied using an infrared radiant spot heater that concentrated thermal

energy to a 13 mm (.5 in) diameter spot at the center of the test specimen. Thermal and mechanical loading variables were investigated for test durations of five minutes. At the completion of the tests, the damage and failure mechanisms were recorded.

A detailed description of the experimental methods and theoretical analysis of the results is presented in the following chapters. Chapter 2 presents a brief description of the experimental equipment and safety precautions used. Chapter 3 describes the thermal loading and combined loading test methods and the results of thermal and mechanical damage from these tests. An analysis incorporating the degradation in fiber microbuckling strength and the presence of a stress concentration, as well as an evaluation of the experimental data, are explored in Chapter 4. Chapter 5 concludes with a summary of the results, conclusions and recommendations for future work.

## Chapter 2 Experimental Equipment

### 2.1 Material Specimens

The test specimens consisted of Micarta G-10 FR-4, which is a flame retardant grade E-glass/epoxy laminate with high mechanical strength, good electrical properties and excellent moisture resistance. It is used for structural members, slot insulation, wedges and panels [12]. The G-10 FR-4 specimens were composed of [0/90] woven plies and fabricated from 3.20 mm x 914 mm x 1220 mm (0.125 in x 36.0 in x 48.0 in) sheets through a proprietary curing process by International Paper. The 3.20 mm (0.125 in) thick plates were then cut using a diamond cutter to a specimen size of 102 mm (4 in) wide by 127 mm (5 in) long.

The resin used in this material was a brominated bisphenol-A epoxy-based vinylester resin diluted in a styrene monomer. The effects of the brominated epoxy are to improve elevated temperature performance and to provide chemical resistance and flame retardation [13,14]. Elevated temperature resistance of brominated epoxies is achieved through an increased glass transition temperature ( $T_g$ ). Where nonbrominated G10 laminates have a  $T_g$  of approximately 100 °C (212 °F), brominated G10 laminates have a  $T_g$  of approximately 130 °C (266 °F). Further material properties of the laminate are given in Table 2.1 [13].

**Table 2.1 Mechanical Properties of Micarta G10 FR4**

Density, g/cm <sup>3</sup> (lb/in <sup>3</sup> )	Compressive Strength, MPa (ksi)	Flexural Modulus, GPa (Msi)	Glass Weight Fraction, %	$T_g$ , °C (°F)
1.91 (.069)	241 (35)	19.3 (2.8)	55	130 (266)

The specimen size was determined by the loading capacity of the testing machine, material availability, and the conductivity characteristics of the material. Due to the maximum loading capacity of the machine and the availability of material, the size was of a much smaller scale than that of the material's proposed application. However, while reduced, the size had to be large enough to maintain the goal of localized thermal loading. Therefore, the material specimen was made wide enough to provide a sufficient  $a/w$  ratio of approximately 0.25 (where  $a$  is the diameter of the heat zone and  $w$  is the material width). The length also had to be long enough to provide a sufficient  $a/l$  ratio of approximately 0.25 (where  $l$  is the material length), yet short enough to minimize global buckling effects. Finally, the thickness was optimized to allow for minimal global buckling effects and maximum temperature uniformity in the through thickness direction. This parameter was determined through initial thermal loading tests.

## 2.2 Mechanical Testing Apparatus

### 2.2.1 Compression Test Fixture

The specimens were held aligned in the testing machine using aluminum fixtures. The material specimens were loaded in compression by clamping two of the edges into the fixtures while the other two remained free. As shown in Figure 2.2, the short edges of the specimen were constrained by the specimen fixtures, which were grooved clamps used to hold the specimen in place while a load was applied. The fixtures were machined from aluminum stock and contained grooves 114 mm (4.5 in) in length, 6.35 mm (.25 in) in width and 12.7 mm (.5 in) in depth (see Appendix A for detailed drafts). The remaining space in the grooves was taken up by steel shims. The bottom clamps were bolted to a base plate that was then attached to the base of the testing machine (Figure 2.1). The top clamp was threaded to an adapter that attached to the load cell of the testing machine.

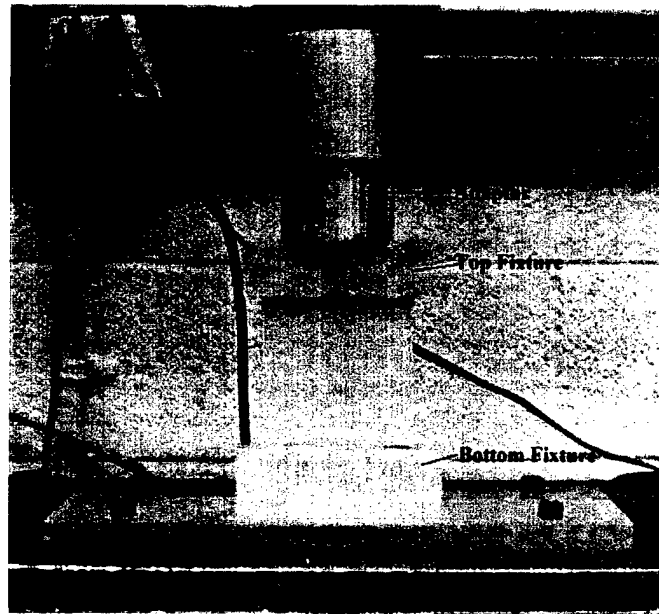


Figure 2.1 Compression test fixture

### **2.2.1 Instrumentation and Testing Machine**

Instrumentation consisted of a load cell (22 kN capacity) and a displacement transducer integrated with the Instron 5500 Series materials testing machine. Positioning of the crosshead is repeatable to within 1.0 micrometer [15].

## **2.3 Thermal Equipment**

### **2.3.1 Infrared Radiant Spot Heater**

A high temperature and industrial quality heat gun was initially used as a thermal loading source. The heat gun had temperature control capabilities and the heat was focused using a 0.635 cm (0.25 in) adapter on the end of the nozzle. Preliminary tests found that the heat flux was inconsistent and non-uniform. The high speed flow from the gun resulted in an impinging jet of energy, where most of the heat was convectively forced along the material surface extending the heated region further than desired. In addition, the temperature range was found inadequate in providing sufficient thermal loading to cause damage to the material.

Further investigations resulted in the choice of an infrared radiant heater to be the most adequate and appropriate source of thermal loading. Using a Model 4150 electric infrared spot heater produced by Research, Inc., localized thermal loading was obtained. The spot heater is designed to provide clean, non-contact heat on a small target or object. It uses a high intensity, short wave infrared emitter to supply a range of concentrated energy to a 13.0 mm (0.5 in) 'spot' approximately 25.0 mm (1 in) from the end of the heater collar (Figure 2.2).

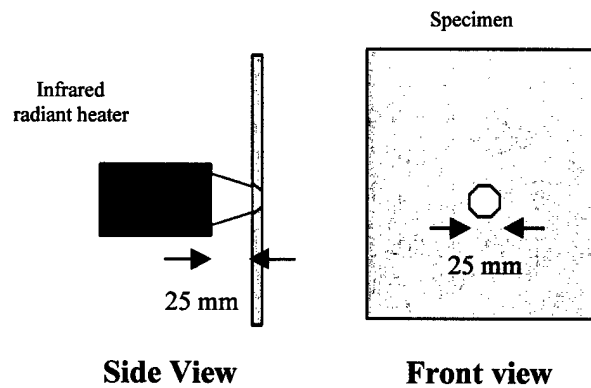


**Figure 2.2** Concentrated thermal energy produced by the infrared heater.

The heater was controlled by a Model 5620 power controller which manually set the voltage into resistive loads. The power controller provided a smooth application of power to the load from 0 to 100 percent of the line voltage. By adjusting the power setting on the controller, the energy output of the lamp was linearly controlled and resulted in variable heat fluxes ranging from  $85 \text{ kW/m}^2$  to  $195 \text{ kW/m}^2$  for the predetermined spot size of 13.0 mm (0.5 in). The heater was fastened to an adjustable platform that allowed for variable height and distance positioning. A Coleman air pump was used to supply the necessary 2.83 CMH (100 CFH) of cooling air to the heater.

### **2.3.2 Radiometer Calibration**

The heater calibration was conducted using a water-cooled Schmidt-Boettler type radiometer. The radiometer was placed 25 mm (1 in) from the heater and aligned with the center of the emitter. Voltage readings were recorded in increments of .5 for heater settings between 0 and 2.5. These voltages were converted into heat flux measurements and a linear approximation was derived from the points. The calibration equation used to

determine the heat flux was  $y = 19.64x$ , where  $x$  is the voltage in mV and  $y$  was the heat flux in  $\text{kW/m}^2$ . The calibration curve is shown in Figure 2.3.

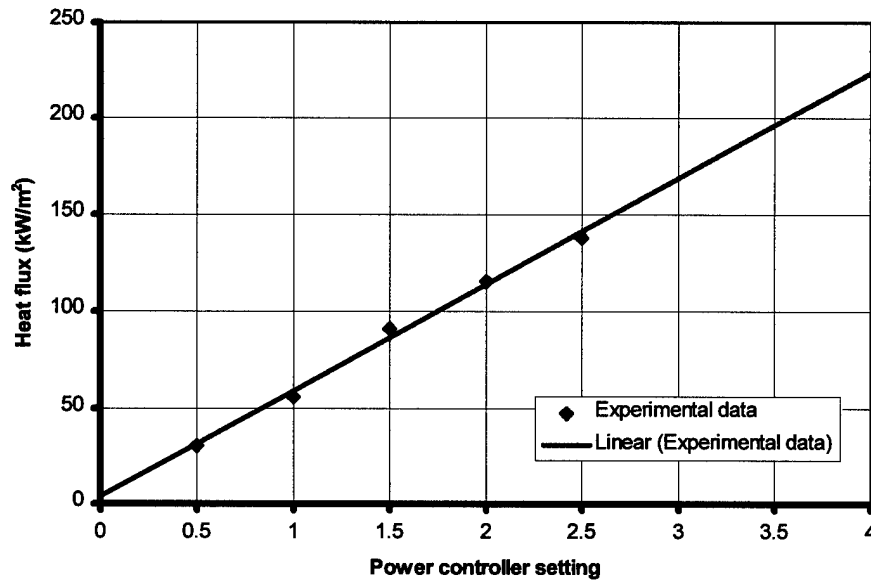


**Figure 2.3 Infrared spot heater calibration at a distance 2.54 cm from the heater collar.**

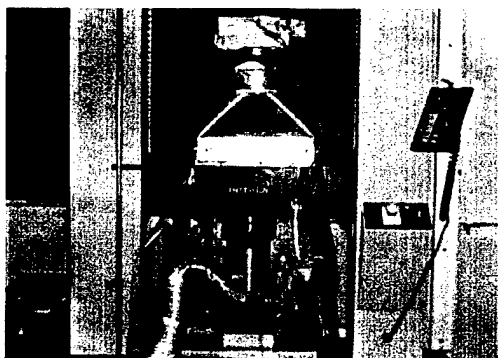
### **2.3.3 Infrared Camera**

Thermal data was taken using a ThermoCAM, a handheld infrared imaging radiometer. The ThermoCAM is a thermal imaging and measurement system with full screen measurement and image storage and analysis capabilities. Using this camera, thermal images were taken to determine the in-plane temperature distribution through the material. An emissivity of 0.90 for the laminate was assumed and thermocouples were used to verify the initial temperature readings of the camera. The thermal images were stored on removable SRAM PCMCIA memory cards and were later output to a software program which enabled the user to image the infrared profiles and plot the temperature distribution across the specimen.

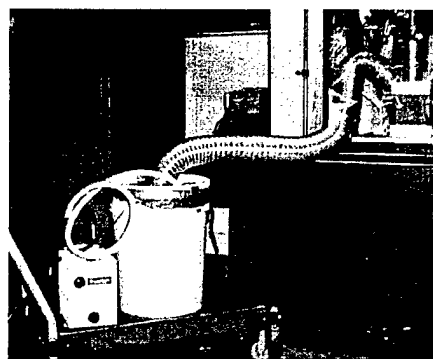
## **2.4 Safety Precautions**

Heating of the test specimens above 450° F results in the release of potentially hazardous pyrolysis products. These products include carbon monoxide, carbon dioxide, and hydrocarbons that irritate the nose, throat and lungs if inhaled for a significant duration [16]. In order to control the dissipation of these vapors and maintain a safe testing environment, a portable ventilation system, Figure 2.5, was developed and a ventilation mask was used.

The ventilation system captured the fumes by first isolating the testing area through the use of a hood with plastic curtains which hung down from the Instron crosshead and surrounded the testing area. A charcoal filter was incorporated into the top portion of the hood in order to assist in filtering the fumes. A vacuum pump was used to draw the fumes from the test area, through ducting and into a sealed bucket containing an ammonia-water mixture. In the mixture, the pyrolysis products recombined and the excess gases were extracted by the pump. These gases were fed through the pump and exhausted through tubing to the outside. A vapor mask was also used as a secondary precaution. Due to the minimal fumes created and the portability necessitated by the testing facilities, an afterburner was not used in the system.



(a)



(b)

**Figure 2.4** Portable ventilation system: (a) hood with plastic isolation curtains and (b) vacuum pump system for filtering combustion products.

## ***Chapter 3 Experimental Methods and Results***

### **3.1 Introduction**

Here the defined parameters and test methods conducted to determine the compressive behavior of composite laminates subjected to thermal loading are presented. The first section is a description of the four parameters considered in the tests. These parameters include the size of the test specimen, the applied compressive load, the applied thermal load, and the duration of testing. The second section includes a detailed description of the test method and results for the unloaded thermal tests. These tests consisted of thermally loading the specimens in order to isolate the damage created solely by thermal loading and to determine the temperature distributions through the in-plane direction of the material at various heat fluxes. The third section is a description of the test method and results of the combined thermal and mechanical loading tests. In these tests, the material specimens were loaded to a constant compressive load and then subjected to a constant applied thermal load.

## **3.2 Testing Parameters**

### **3.2.1 Specimen Geometry**

The specimen geometry remained constant throughout the reported tests. As mentioned previously in Chapter 2.1.1, the geometry was determined by machine loading capacity, the buckling characteristics and the thermal characteristics of the material. Preliminary tests were conducted using laminates with dimensions of 102 mm (4 in) by 305 mm (12 in) and a thickness of 6.40 mm (.25 in). These tests found that the 6.40 mm (.25 in) thick specimens were too thick to be significantly affected by the tested heat fluxes and that failure was predominantly through global buckling. Thinner specimens of 101 mm (4 in) by 127 mm (5 in) and a thickness of 3.20 mm (0.125 in) were then selected and shown to have more uniform temperature distributions through the thickness direction as well as a greater susceptibility to mechanical and thermal degradation at the tested loads.

### **3.2.2 Applied Compressive Load**

The applied compressive load was held constant for each test. Tests were conducted for a given thermal load where the compressive load was increased in 900 N (200 lb) increments until the global buckling load was approached. Near or at the global buckling load, the applied load was increased in 445 N (100 lb) increments until failure of the specimen. Failure was defined as the instance where the material specimen could no longer support the applied load.

The global buckling load of the material was determined using Euler's buckling equation for a rectangular cross-section, defined in Equation (1.1). Using an end factor of  $k=.75$  to approximate the support conditions, an approximate theoretical buckling load

was determined for a specimen size of 3.20 mm x 102 mm x 102 mm (.125 in x 4 in x 4 in), loaded axially along the length. The decreased specimen length of 102 mm (4 in) used in determining the theoretical value is due to the decrease in effective length caused by the design of the testing fixture. An approximate Young's Modulus of 20.7 GPa (3.0 Msi) was used in calculations. Calculations of the buckling approximation are shown in Appendix B.

Experimental measurements were then conducted to verify the buckling calculations. The specimen was loaded to failure on a 89 kN (20,000 lb) capacity testing machine at a crosshead rate of 0.011 mm/sec (0.025 in/min). The theoretical and experimental buckling approximations showed good agreement and are listed in Table 3.1.

**Table 3.1: Buckling Load of Micarta G10 FR4**

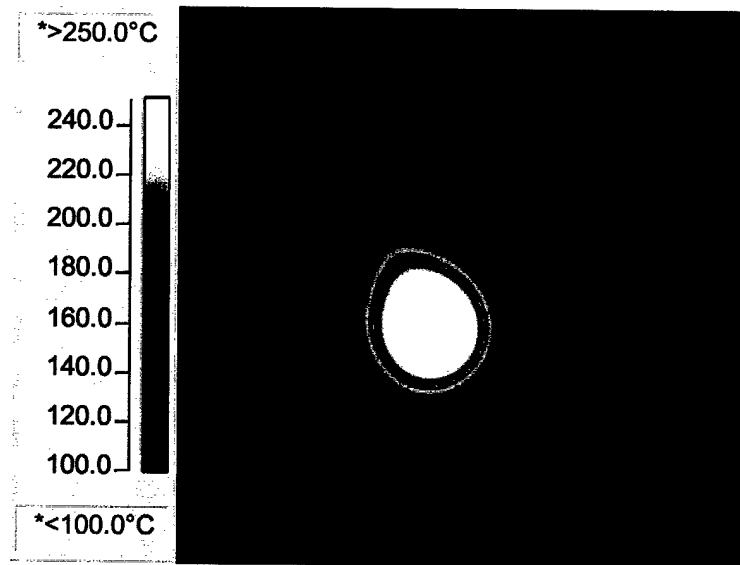
Material	Young's Modulus, GPa (Msi)	Theoretical Buckling Load, N (lbs)	Experimental Buckling Load, N (lbs)
Micarta G-10 FR-4	20.7 (3.0)	9530 (2140)	10230 (2300)

### 3.2.3 Applied Thermal Load

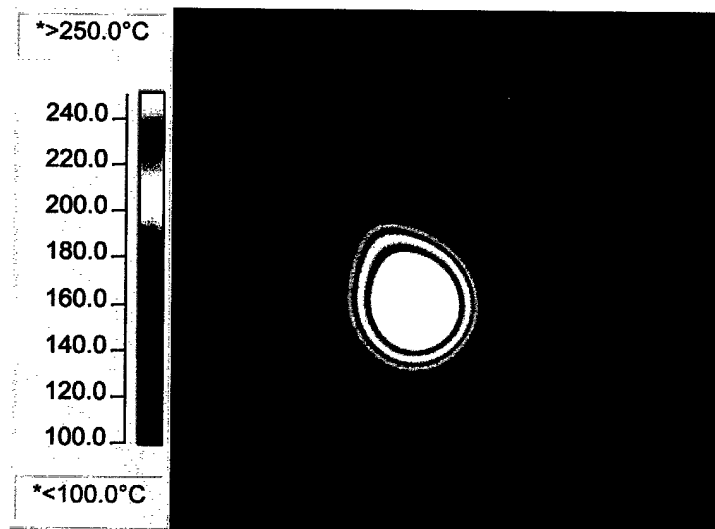
Three series of tests were run at three levels of thermal loading to simulate the conditions for a compartment fire of approximately 100 kW/m<sup>2</sup>. The heat fluxes selected were 85 kW/m<sup>2</sup>, 140 kW/m<sup>2</sup>, and 185 kW/m<sup>2</sup>. For each value of loading, the energy was focused to a 13.0 mm (.5 in) diameter spot on the surface of the specimen. The actual heat affected zone created by this loading varied for each heat flux due to conduction through the material. These heat fluxes were held constant throughout the duration of the test.

### **3.2.4 Test Duration**

The test duration remained constant for each test. It was measured from the initiation of thermal loading and concluded after a lapsed time of five minutes. Based on thermal imaging measurements, the temperature distribution stabilized after approximately four minutes. This stabilization is due in part to the energy losses through the material and the insulating effects of the charred region of material that results from high intensity thermal loading. With these factors in mind, a maximum test time was set at five minutes. Figure 3.1 shows the stabilization of the temperature distribution for a specimen exposed to four minutes of thermal loading and a specimen exposed to five minutes of thermal loading. It can be seen from this figure that the temperature zones for each specimen are approximately equal. Therefore, it was assumed that no significant change in temperature distribution occurred after five minutes and the amount of thermal damage had reached a maximum.



(a)



(b)

**Figure 3.1 Thermal images showing stabilization of temperature distribution from (a) 4 minutes of exposure to (b) 5 minutes of exposure at a heat flux of  $140 \text{ kW/m}^2$ .**

### **3.3 Unloaded Thermal Tests**

#### **3.3.1 Method**

Thermal tests were conducted on unloaded specimens in order to isolate and characterize the damage created by thermal loading alone and to determine the temperature distribution in the in-plane direction of the specimen during various thermal loading conditions.

Using the lower compression fixture grips, specimens were held stationary by one edge. The infrared heater was placed 25.0 mm (1 in) from the face of the plate and focused on the center of the plate (Figure 3.2). The ThermoCAM infrared measurement system was used to record the temperature distribution in the in-plane direction of the plate during the tests. As shown in Figure 3.2, this camera was placed opposite the heater on the unexposed side of the plate. The camera was arranged in this manner due to the obstruction of the view by the heater on the exposed side of the specimen. These tests were conducted under a fume hood in order to minimize inhalation hazards.

The test consisted of applying a constant heat flux to the plate for a duration of five minutes. Using the ThermoCAM, thermal measurements of the unexposed face were taken during the test. These thermal images were recorded at one-minute intervals. At the conclusion of the test, the physical damage was recorded. This process involved physically measuring the diameters of the charring and delamination areas using calipers. This test was conducted for three thermal loading conditions: 85 kW/m<sup>2</sup>, 140 kW/m<sup>2</sup> and 195 kW/m<sup>2</sup>.

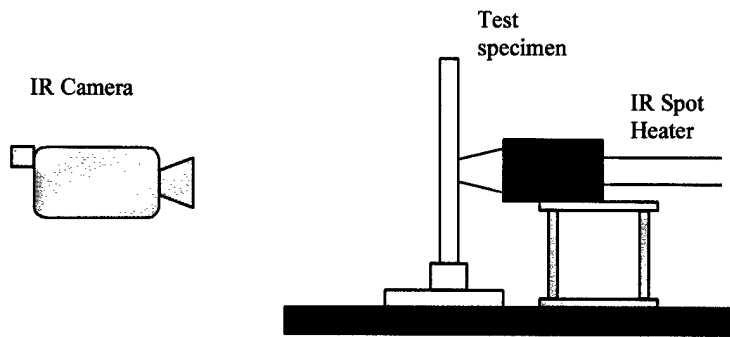


**Figure 3.2 Thermal loading schematic**

### **3.3.2 Infrared Images**

The infrared images recorded the temperature distributions in the in-plane direction of the back side of the specimen. Positions on the test specimen were determined using an image alignment tool from the thermal imaging software. This tool allowed the same measurements to be taken for a series of images of the same specimen or of the same dimensions. Using the alignment tool, temperature distributions as a function of distance from the loading spot were determined and comparisons of the temperature profiles from each of the three loading conditions were compared. Due to the relative thinness of the plate and the small temperature gradient through the thickness, the temperature profiles were approximately equal between the unexposed surface and the exposed surface of the specimen.

Temperature distribution images at the five-minute interval are shown in Figure 3.3 for each of the heat fluxes tested. These images use a color-coded temperature scale to show the distribution in the in-plane direction of the specimen. The span was limited to an optimum range of 100 °C (212 °F) to 250 °C (482 °F). Due to the convective effects of the hood exhaust system, the temperature profile is slightly asymmetrical.

Temperature distribution plots were derived from the image data and are shown in Figure 3.4. These plots show the temperature as a function of distance from the center of the test specimen, where the thermal loading was focused. Due to the limitations of the camera imaging range, temperatures readings above 320°C (608 °F) could not be measured and therefore, the temperature profiles in the Figure 3.4 plateau at 320°C (608 °F). This limitation does not indicate that temperatures experienced by the specimen did not exceed 320°C, it just means that this was the maximum temperature recordable.

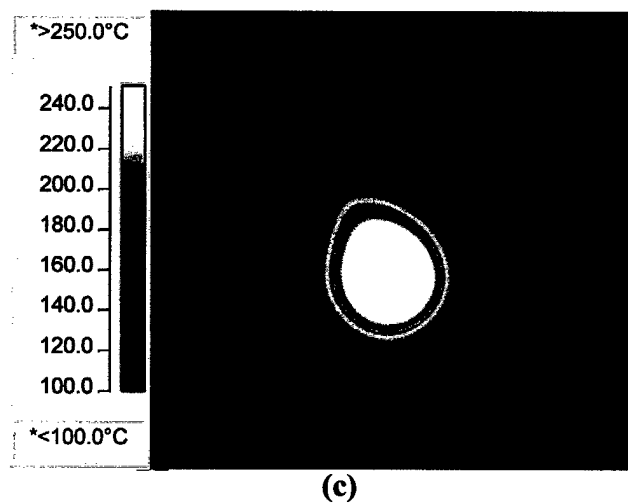
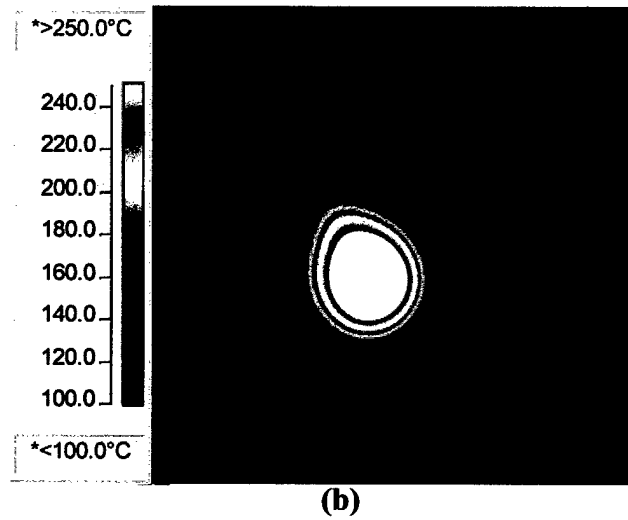
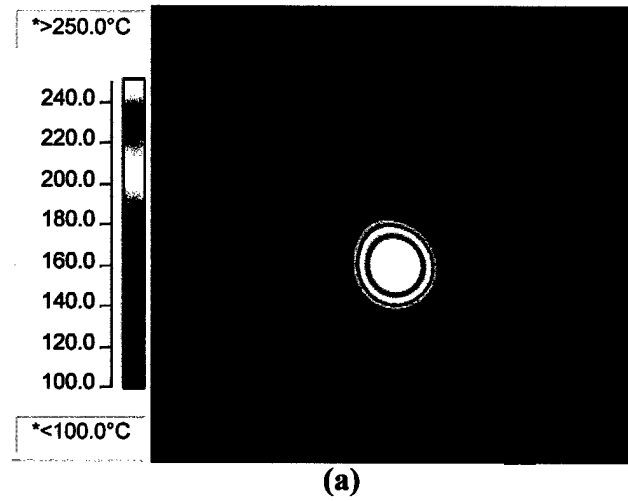


**Figure 3.3** Temperature distribution of specimens at five minutes of exposure for thermal intensities of (a)  $85 \text{ kW/m}^2$ , (b)  $140 \text{ kW/m}^2$ , and (c)  $195 \text{ kW/m}^2$ .

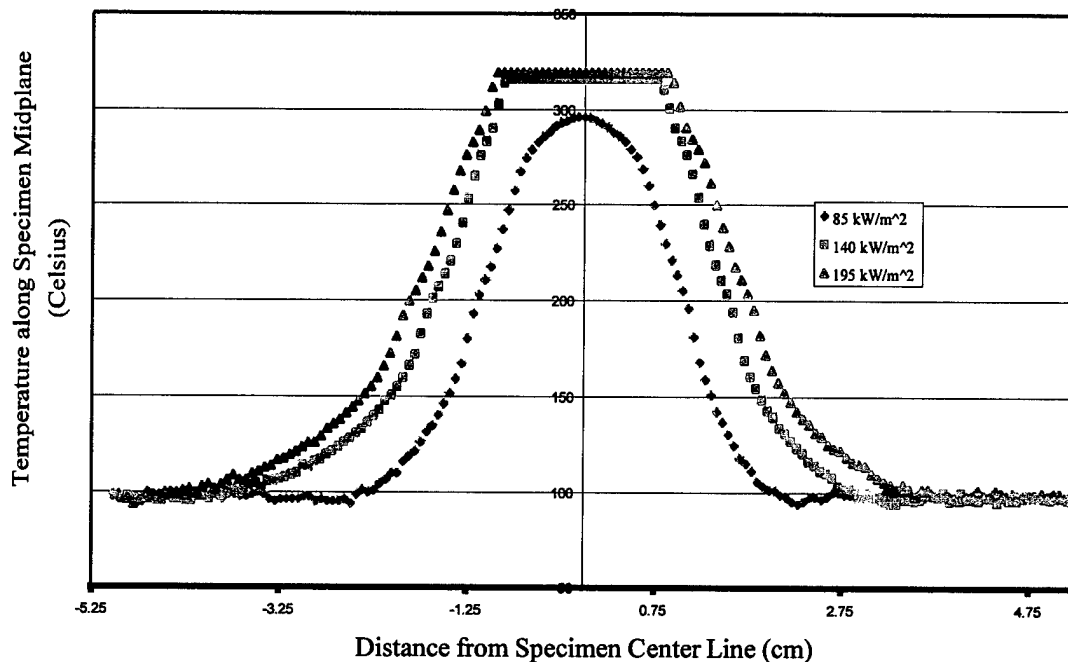


**Figure 3.4 Temperature distribution at the specimen midplane after five minutes of thermal loading at specified heat fluxes. Temperature plateaus at 320 C are due to the range limitations of the thermal imaging equipment.**

### 3.3.3 Material Damage

Thermal loading of the test specimens resulted in physical damage in the form of delamination and charring. Delamination of the composite occurred first on the exposed side of the material in the concentrated area of thermal loading within 30 seconds of heating. This delamination spread radially with the conduction of heat through the in-plane direction. As heat was conducted through the thickness of the material, delamination occurred on the unexposed side of the material. As the thermal loading continued, the material experienced charring of the laminate matrix. This charring extended radially outward in-plane from the center of concentrated thermal loading. As the material began to char and the heat transfer through the material began to stabilize at

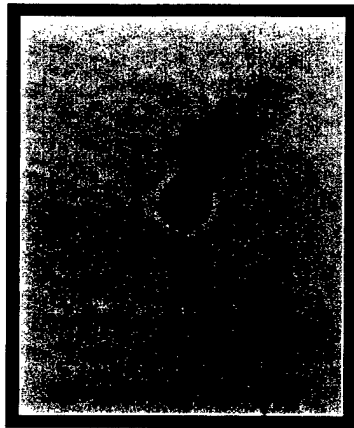
approximately three minutes, growth of the damage area ceased. Tables 3.2a – 3.2b list the damage created at each heat flux on both the unexposed and exposed surfaces of the material. Photographs of the physical damage on both the exposed and unexposed surface of the material are shown in Figure 3.5 for each loading condition. The vertical dark region that appears on the specimens is soot deposited due to the vertical entrainment of smoke by the hood exhaust system.

**Table 3.2a Thermal damage of exposed surface**

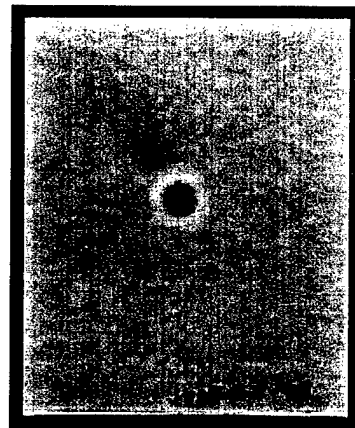
Heat Flux (kW/m <sup>2</sup> )	Charring diameter (mm)	Delamination diameter (mm)
85	20.6	23.8
140	25.4	28.6
195	28.6	31.8

**Table 3.2b Thermal damage of unexposed surface**

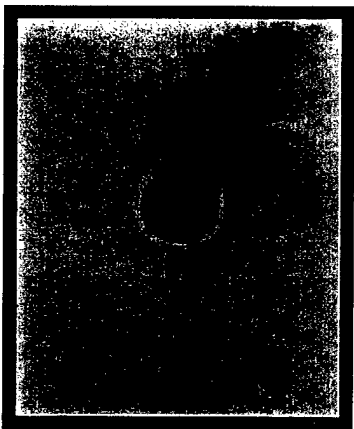
Heat Flux (kW/m <sup>2</sup> )	Charring diameter (mm)	Delamination diameter (cm)
85	15.9	22.2
140	22.2	27.0
185	25.4	28.6



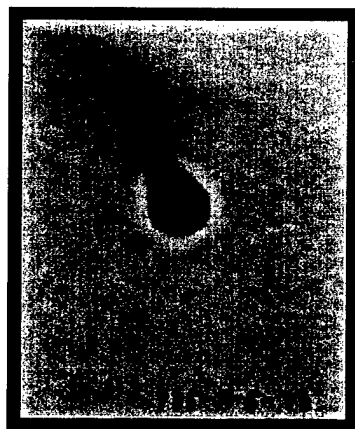
(a1)



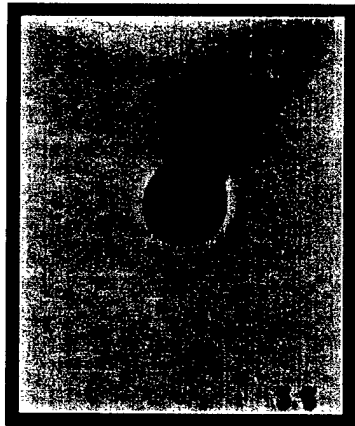
(a2)



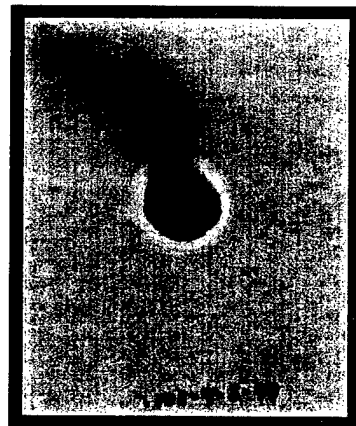
(b1)



(b2)



(c1)



(c2)

**Figure 3.5** Damage of exposed and unexposed specimen surfaces due to solitary thermal loading at various heat fluxes: (a1)  $85 \text{ kW/m}^2$ , exposed surface, (a2)  $85 \text{ kW/m}^2$ , unexposed surface; (b1)  $140 \text{ kW/m}^2$ , exposed surface, (b2)  $140 \text{ kW/m}^2$ , unexposed surface; (c1)  $195 \text{ kW/m}^2$ , exposed surface; (c2)  $195 \text{ kW/m}^2$ , unexposed surface. The dark plumes of soot are due to the vertical entrainment of smoke by the hood exhaust system.

### **3.4 Combined Loading Tests**

#### **3.4.1 Method**

In these tests, thermal and compressive mechanical loads were applied to the specimens simultaneously using the Instron mechanical testing equipment and the infrared heater.

First, the specimen fixtures were secured to the Instron testing machine, centered with the base plate and the load cell. The specimen was then placed in the bottom fixture and aligned with the center of the fixture. Steel shims were placed on either side of the specimen to secure and center the specimen in the fixture. The top fixture, attached to the load cell and crosshead, was then lowered slowly and aligned with the specimen. The top fixture was lowered carefully while the specimen was inserted approximately 2.5 mm (0.1 in) into the fixture notch (Figure 3.6). At this point, steel shims were inserted in between the specimen and the top fixture to secure the specimen in position. The top fixture was then lowered slowly until there was an initial detection of the compressive forces, at which point the crosshead was raised slightly to release the load. The extension and load measurements read by the software data acquisition system were then calibrated to zero.

Once the specimen had been positioned in the testing machine, the infrared heater was positioned and aligned with the specimen. The heater was secured to its adjustable platform and placed on the side of the machine baseplate, facing the specimen (Figure 3.7). The platform was then adjusted to position the heater collar 25.0 mm (1 in) from the specimen and to center it on the specimen (Figure 3.7).

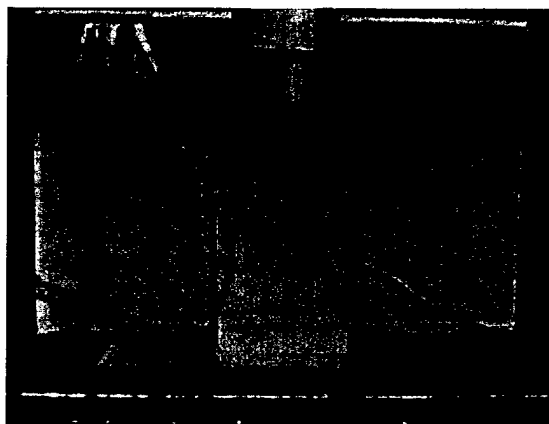
The ventilation curtains were placed on the top of the crosshead and the ducting was secured to the crosshead and positioned near the top fixture in order to capture fumes efficiently (Figure 3.8).

Prior to beginning the tests, the Merlin software was programmed. The specimen number and dimensions were entered and the crosshead rate, the rate at which the crosshead was lowered, was set to .0106 mm/sec (.0025 in/min) for every test. The load was programmed to reach and maintain a constant compressive load. As stated previously, these loads were varied for each test.

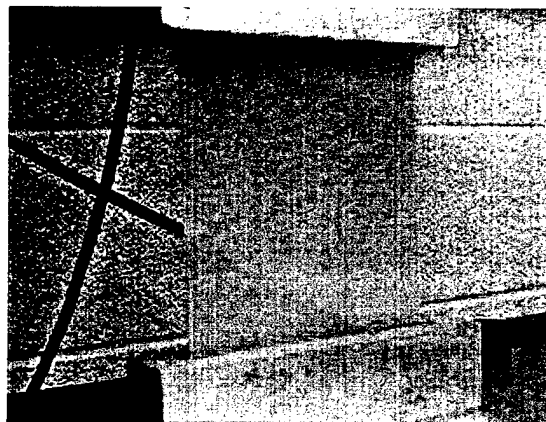
Testing began by initiating movement of the crosshead. As the crosshead was lowered, the compressive load applied to the specimen increased. As this load approached the constant compressive load, the heater was positioned to idle and the ventilation system was turned on. When a constant load was reached, the full thermal load was applied and the timer was started.

During the test, the extension and load data was captured the testing machines data acquisitions program. Visible damage was also recorded. At the completion of five minutes or global collapse of the specimen, whichever occurred first, the test was concluded. Thermal loading was stopped and mechanical loading was released. The visible physical damage was then measured and recorded. After all measurements were recorded, the specimens were placed in sealed plastic bags.

This method was repeated for a series of tests at each of the stated heat flux values.

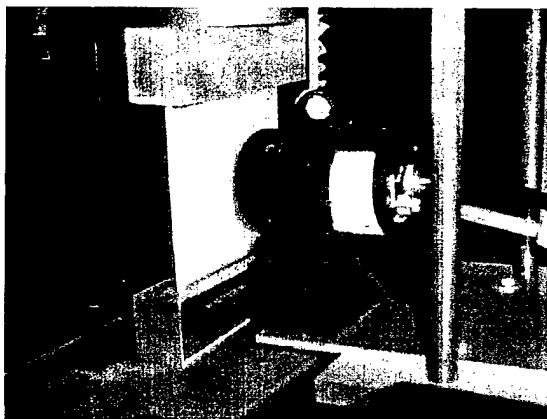


(a)

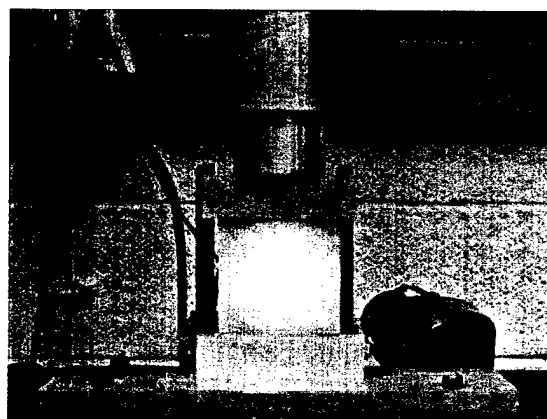


(b)

**Figure 3.6** Placement of test specimen in the compression testing fixtures: (a) the alignment of the test specimen in the bottom fixture and (b) the alignment of the top fixture with the specimen edge, prior to insertion of the specimen into the top fixture.



(a)



(b)

**Figure 3.7** Alignment of spot heater with test specimen: (a) positioning of heater on load machine baseplate and (b) energy concentration centered on the test specimen.

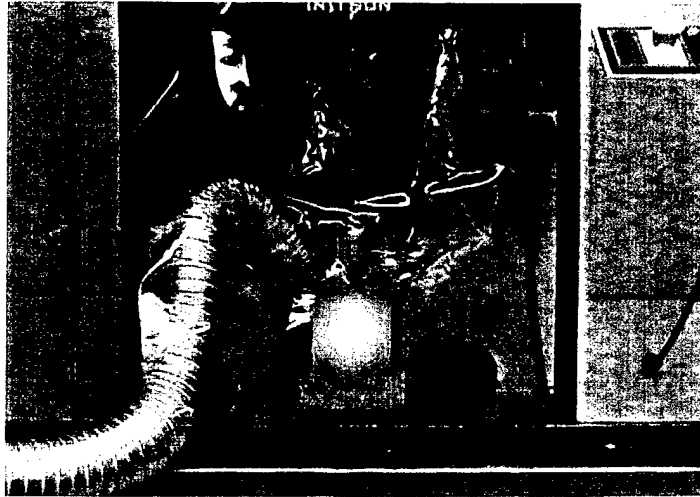


**Figure 3.8 Ventilation system with curtains and fume ducting.**

### **3.4.2 Combined Loading Test Results**

The visible initiation of physical damage was recorded during the tests and the final damage was recorded at the conclusion of each test. The main forms of damage consisted of laminate delamination, matrix charring, microbuckling and global failure. A schematic displaying the failure modes of microbuckling and delamination is shown in Figure 3.9. The lengths  $m_f$  and  $m_r$  are the microbuckling lengths on the front and rear surfaces of the specimen. The diameters  $d_f$  and  $d_r$  are the delamination diameters on the front and rear surfaces.

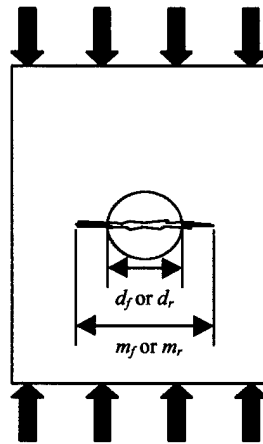


**Figure 3.9 Schematic of failure modes observed**

It was noted from observations that, for each of the applied heat fluxes, delamination initiated on the exposed surface of the specimen within the first 30 seconds of thermal loading. This delamination originated at the center of the concentrated thermal loading zone (the “spot”) and spread radially outward on the surface. Delamination of the unexposed surface followed delamination of the exposed surface and, generally, encompassed a smaller area than delamination on the exposed surface. The diameter of the delaminated region tended to increase with an increase in thermal loading (Figure 3.10). However, for a given thermal load, this diameter did not change with an increase in compressive load. It was also observed that for the tests conducted at lower intensities of compressive loading delamination preceded any other form of damage.

Charring of the material matrix occurred after delamination was initiated, as the material thermally decomposed. The charring spread radially outward in the in-plane

direction and through the thickness of the material. The area of charring was consistent for a given heat flux and did not change with a change in applied load (Figure 3.11).

Microbuckling was observed to initiate within the concentrated thermal loading zone and propagated horizontally from the center outwards along the midplane of the specimen. The length and thickness of the microbuckling region tended to increase with both an increase in applied thermal load and an increase in applied compressive load. The microbuckling length refers to the distance of horizontal propagation across the specimen.

At the initial compressive loads (approximately 1/3 of the specimen buckling load), delamination initiation would precede microbuckling initiation. The initiation of microbuckling was difficult to visibly detect at these loads due to the effects of delamination. The length of microbuckling was also generally less than the diameter of delamination at these initial loads. As the applied compressive load increased, the length of microbuckling increased to greater than the delamination diameter. Eventually, at the higher compressive loads, microbuckling was initiated before delamination. At or near the global buckling load of the specimen, microbuckling reached a critical length, Euler buckling occurred and the specimen collapsed globally.

Figure 3.12 shows the development of microbuckling for specimens thermally loaded at  $140 \text{ kW/m}^2$ . A comprehensive description of the material damage for specimens tested at the three thermal loading conditions under various compressive loads is given in Appendix C. The damage is reported in ratios, where the length of damage is normalized by the width of the specimen.



**Figure 3.10** Delamination and charring regions of specimens subjected to a compressive load of 22.1 MPa and heat fluxes of (a) 85 kW/m<sup>2</sup>, (b) 140 kW/m<sup>2</sup>, and (c) 195 kW/m<sup>2</sup>. The dark plumes of soot are due to the vertical entrainment of smoke by the hood exhaust system.

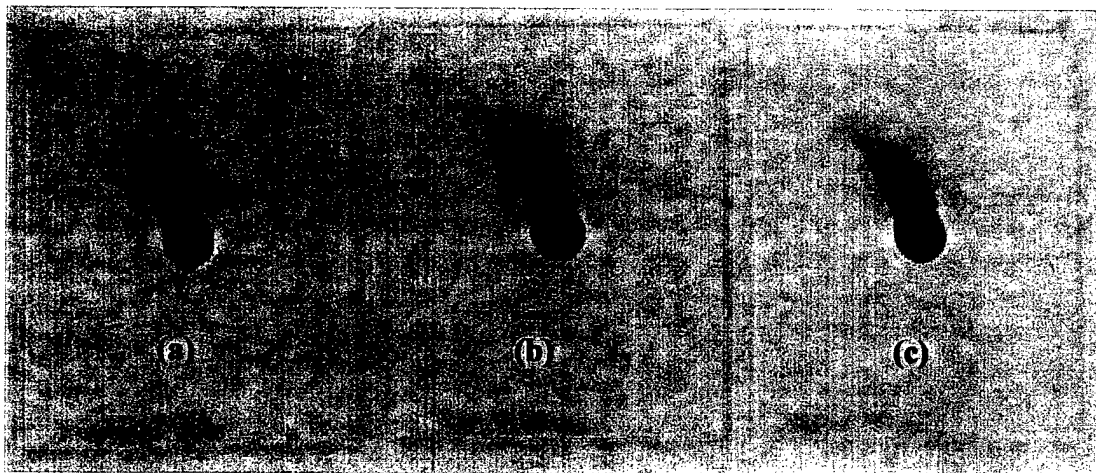
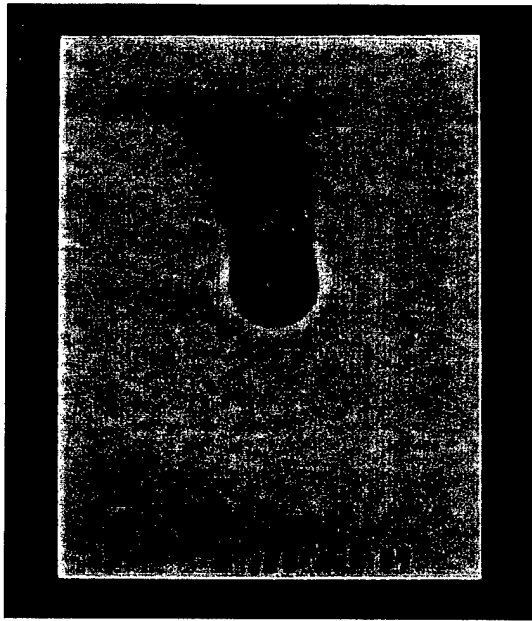
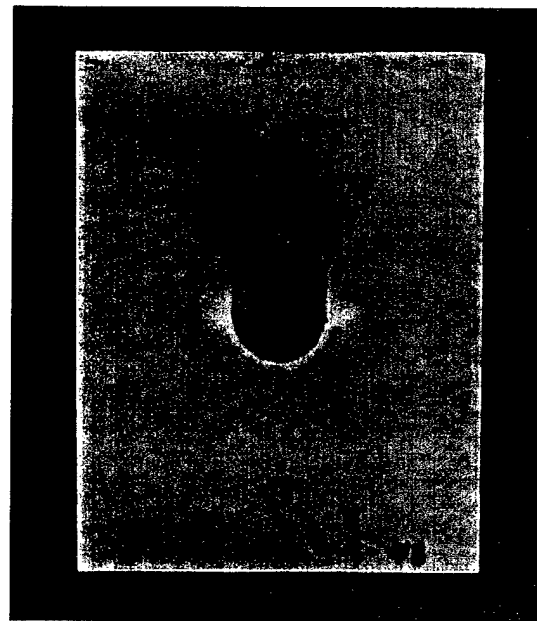


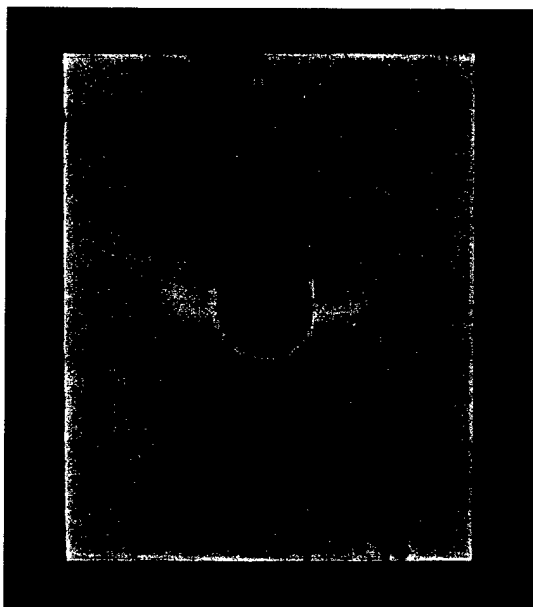
**Figure 3.11** Delamination and charring regions of specimens subjected to a constant heat flux of 85 kW/m<sup>2</sup> and a compressive load of (a) 16.5 MPa, (b) 19.3 MPa, and (c) 22.1 MPa. The dark plumes of soot are due to the vertical entrainment of smoke by the hood exhaust system.



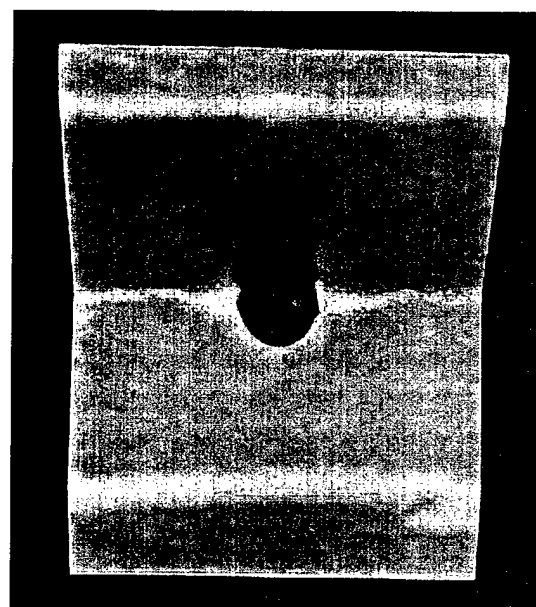
(a)



(b)



(c)



(d)

**Figure 3.12** Progression of microbuckling damage with increasing applied compressive loads for a constant thermal loading of  $140 \text{ kW/m}^2$ : (a) 8.27 MPa, (b) 22.1 MPa, (c) 30.3 MPa, (d) 30.5 MPa. The dark plumes of soot are due to the vertical entrainment of smoke by the hood exhaust system.

## ***Chapter 4 Theoretical Analysis***

### **4.1 Introduction**

The primary modes of failure found in the combined loading tests were delamination, microbuckling and global buckling failure. As will be shown in this section, a comparison of the delamination found in the unloaded thermal tests and the combined loading tests shows similar diameters of delamination for a constant applied thermal load regardless of the applied compressive load. This suggests that delamination was a function of the thermal load, and independent of mechanical loading conditions in these tests. However, microbuckling and global buckling were failure modes absent in solitary thermal loading tests and were introduced through mechanical loading.

These failure modes, microbuckling and global buckling, will be explored in the following section. Their dependence upon combined thermal and mechanical loading conditions makes them a significant factor in the development of a safe, preventive design criterion and it is with this goal that an investigation of their behavior was conducted. By using the temperature data acquired in the solitary thermal loading tests and determining the material properties of the specimens at these temperatures, a reasonable explanation for the presence of these failure mechanisms is obtained.

## 4.2 Background

The dominant mode of failure in compression is by fiber microbuckling. Fiber microbuckling is determined by fiber misalignment, shear modulus, and the shear strength of the composite [10]. As mentioned previously in Chapter 1.2, the shear modulus of the composite is significantly reduced at elevated temperatures. Therefore, with the resulting reduction in interlaminar shear strength and laminate compressive strength, the propensity for fiber microbuckling is increased. The three critical factors in fiber microbuckling failure are: 1) the composite shear modulus, 2) the fiber microbuckling strength, and 3) the matrix glass transition temperature. The following section contains a description of these factors, the correlation that exists between them and their application in the analysis of this research.

The first factor, the composite shear modulus, has two significant components in compressive loading. These are the in-plane shear modulus and the interlaminar shear modulus. The in-plane shear modulus,  $G_{12}$ , can be determined using a strength's of materials approach [10, 17]. From the inverse rule of mixtures, an in-plane shear modulus equation is determined to be

$$G_{12} = \frac{V_m}{G_m} + \frac{V_f}{G_f} \quad (4.1)$$

where  $G_m$  is the matrix modulus,  $V_m$  is the matrix volume fraction,  $G_f$  is the fiber modulus, and  $V_f$  is the fiber volume fraction. When rewritten, the above equation leads to

$$G_{12} = \frac{G_m}{V_m + \frac{V_f G_m}{G_f}} \quad (4.2)$$

in which  $G_{12}$  is a matrix dominated property in the case of stiff fibers. If the fibers are much stiffer than the matrix ( $G_f \gg G_m$ ), the in-plane modulus can be approximated as

$$G_{12} = \frac{G_m}{1 - V_f} \quad (4.3)$$

The interlaminar shear strength,  $G_{13}$ , which acts across the thickness of the composite, is similar to the in-plane shear stress, which acts in the laminate plane and it is generally assumed that

$$G_{13} = G_{12} \quad (4.4)$$

Fiber microbuckling strength is the second factor in microbuckling failure, which is the determining variable of a composite's compressive strength. Rosen [18] developed a mechanics of materials model for local buckling, or microbuckling. Assuming the fibers to be straight, a stability analysis was determined for a shear mode of failure. Shear mode buckling assumes that fibers buckle in an in-phase pattern and the matrix is sheared, rather than an out-of-phase pattern where the matrix is compressed [19].

Rosen's analysis found the buckling stress of the fibers to be

$$\sigma_{CR} = \frac{G_m}{1 - V_f} \cong G_{12} \quad (4.5)$$

As can be seen from Eq. (4.5), the buckling stress is numerically equal to the matrix dominated in-plane shear strength. While this approach gives the most conservative estimate of the buckling strength over a range of practical fiber volume fractions, it still over predicts the buckling strength considerably [10,19]. In order to account for this over prediction, an empirical correction can be made by adding a factor  $k$  which is determined experimentally for a particular volume fraction

$$\sigma_{CR} = \frac{kG_m}{1 - V_f} \cong kG_{12} \quad (4.6)$$

The third factor, the matrix glass transition temperature, dictates the temperature dependence of the matrix shear modulus. The glass transition temperature, or  $T_g$ , is the range in which a polymer goes from a glassy (rigid) behavior to a rubbery behavior [10].

Polymers consist of long molecular chains that are tangled in a liquid-like manner. In the glassy state, these molecules are frozen in crumpled conformations. As the temperature increases, the molecules become more mobile through thermally activated discrete jumps. With this mobility, the molecules are able to change position through increased flexibility, although, the molecular formation does not change [20].

Glass transition of the polymer occurs over a finite temperature interval, however, its change occurs so abruptly that it can be considered a transition. It is recognizable by a change in several material properties, the most important for practical purposes being the decrease in elastic modulus [21]. This reduction in modulus is usually several orders of magnitude. Due to this severe reduction, the  $T_g$  is sometimes referred to as the softening point.

With the previous descriptions, the following scenario can be developed. First, heat is added to a composite material, elevating the material temperature. As the temperature of the material exceeds its glass transition temperature, the matrix modulus decreases by an order of  $10^3$ . This decrease in matrix modulus results in a decrease in the composite shear modulus. In turn, there is a decrease in the fiber microbuckling strength of the composite, which is dependent upon the shear modulus. The decrease in microbuckling strength leads to fiber instability and eventually, failure of the fiber. This scenario is a possible partial explanation for the occurrence and method of microbuckling

observed in the combined loading tests and will be fully investigated in the remaining portions of this section.

### **4.3 Modulus Measurements and Evaluation**

#### **4.3.1 Modulus Measurement through DMA**

The first step in applying the previously described analysis was to determine the modulus of the material at elevated temperatures. The chemistry division of YLA Plastics, an advanced materials fabrication company, conducted these measurements. Using a technique called dynamic mechanical analysis (DMA), the dynamic moduli and damping of the material was measured under an oscillatory load as a function of temperature and frequency as the material was subjected to a controlled temperature program. This technique is a form of relaxation spectroscopy in which the onset of molecular motion and the resulting physical transitions are detected [21]. The shear modulus, storage modulus and tangent of the phase angle of the material as a function of temperature were recorded for a thermal loading of 5 °C per minute. Figure 4.1 displays the shear modulus as a function of temperature. As previously described the modulus experiences a reduction of nearly three orders of magnitude. The measurements were only taken to a temperature of 228 °C. As can be seen from the Figure 4.1, the modulus experiences a sharp decrease at approximately 130°C with little change before and after this transition. The measurements were therefore limited to a maximum temperature of 190°C due to the insignificant modulus changes experienced above this temperature. A complete listing of the data, including the storage modulus and phase angle, are included in Appendix D.

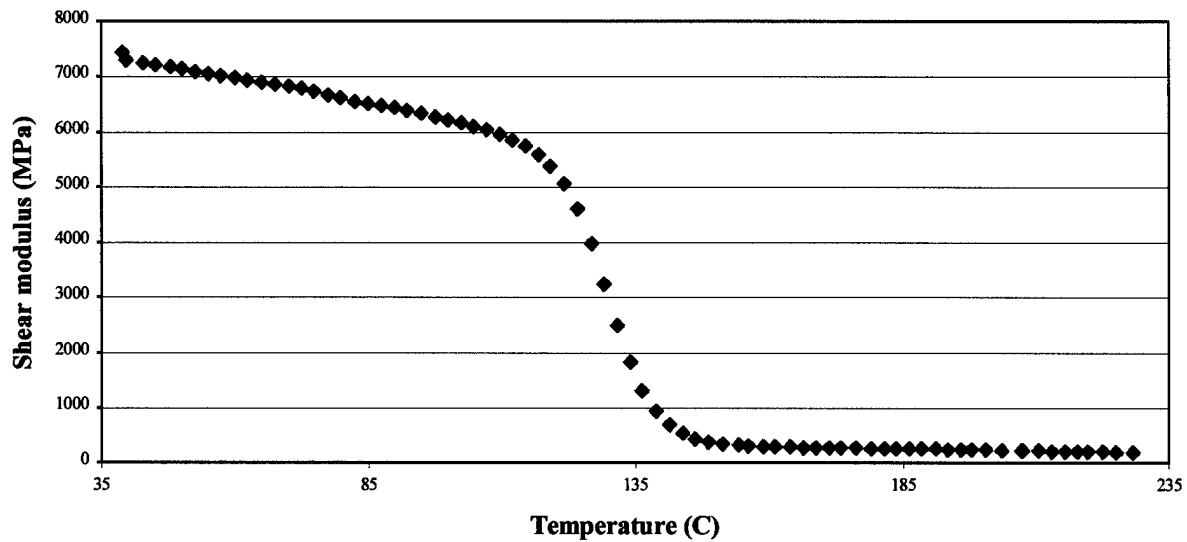


**Figure 4.1 Shear modulus as a function of temperature for Micarta G10 FR4.**

#### **4.3.2 Evaluation of Modulus for Tested Thermal Loading Conditions**

The temperature distribution curves determined from the solitary thermal loading tests were used to determine the shear modulus distribution along the horizontal axis of the specimens for the thermal loading conditions described previously. By plotting both the position versus temperature and the shear modulus versus temperature, the shear modulus versus position could be determined. As shown in Figure 4.2, by using the primary y-axis for the shear modulus data and a secondary y-axis for the position data, positions could be correlated to modulus measurements at corresponding temperatures. Using the data points determined from Figure 4.2, the shear modulus as a function of position for each heat flux was plotted (Figure 4.3). Applying Eqs. (4.5) and (4.6), this figure can also be used to determine the trend of the fiber microbuckling strength.

The data obtained displays a reduction of shear modulus and microbuckling

strength of a factor of approximately 30. This reduction occurs through the glass transition temperature of the material, 130 °C.

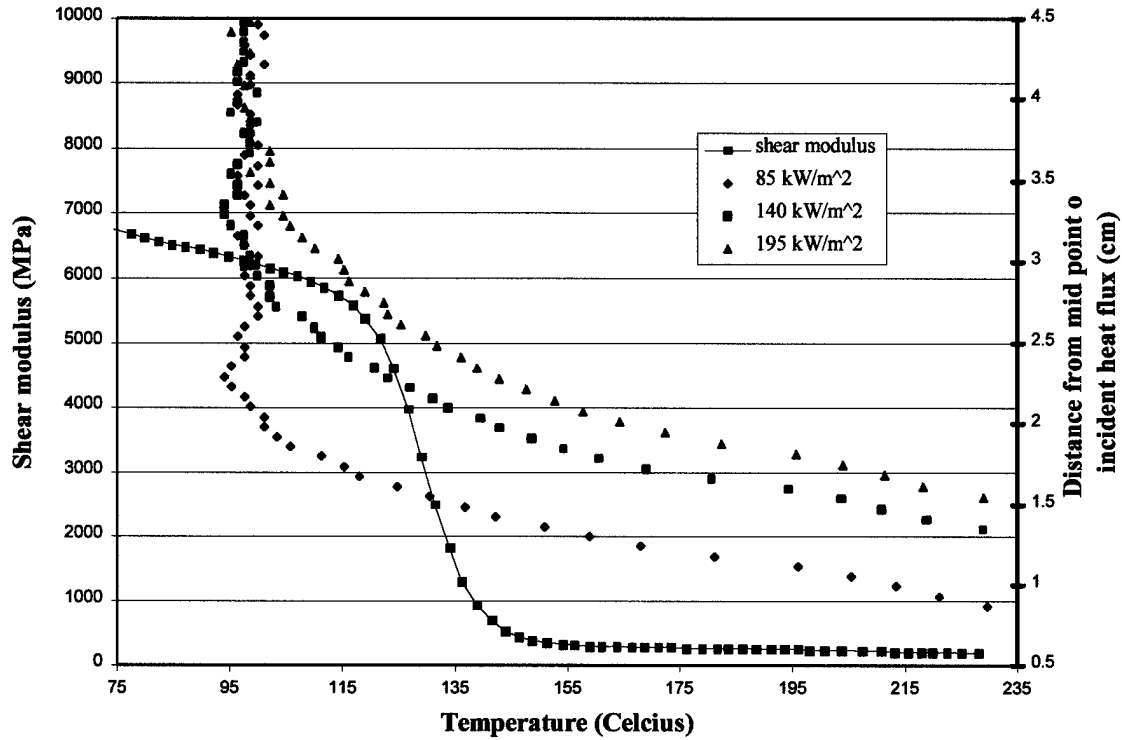


**Figure 4.2** The shear modulus of the material as a function of temperature and the distance position from the specimen midplane for heat fluxes of 70 kW/m<sup>2</sup>, 120 kW/m<sup>2</sup>, and 170 kW/m<sup>2</sup>.

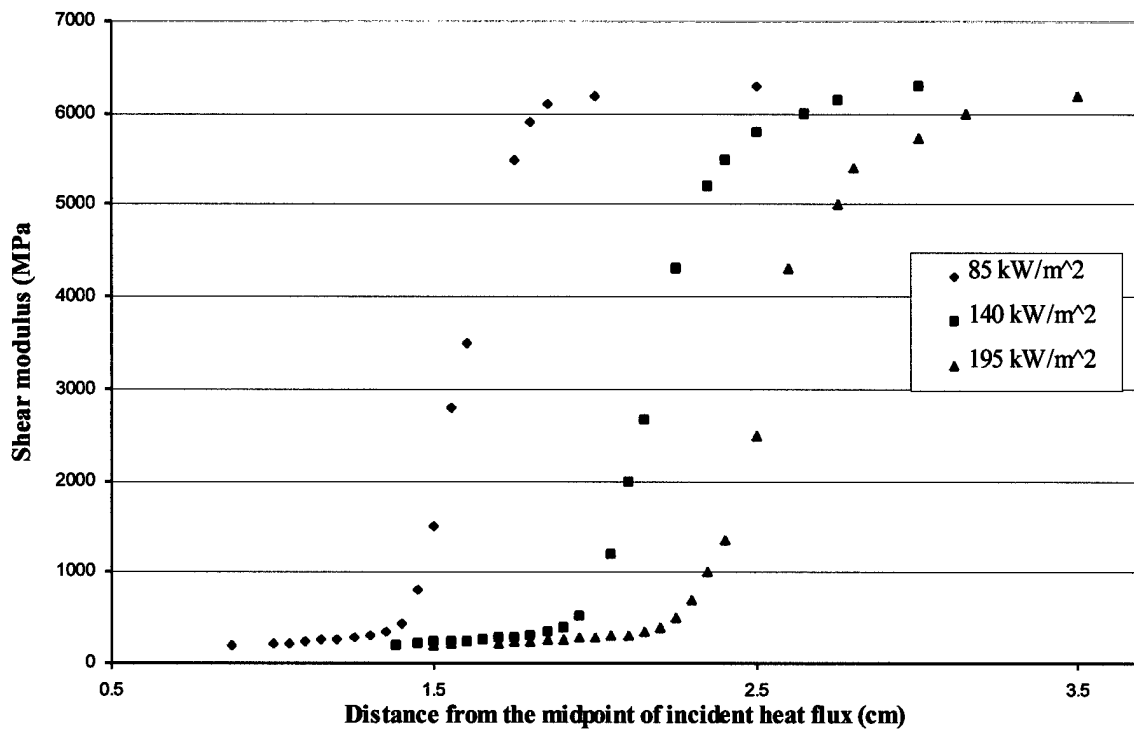


**Figure 4.3** Shear modulus as a function of distance from the midpoint of incident heat flux for heat fluxes of 85 kW/m<sup>2</sup>, 140 kW/m<sup>2</sup>, and 195 kW/m<sup>2</sup>.

## 4.4 Evaluation of Damage

### 4.4.1 Delamination

Delamination and charring damage was fairly constant for each heat flux, regardless of the applied compressive load. This consistency suggests that these forms of damage were primarily a function of the thermal loading condition. The only exception to this observation was in the case of global failure. When global failure was initiated by microbuckling, delamination propagated vertically outward from the inception of global buckling. Table 4.1 shows the average damage measurements on the exposed surfaces for the solitary and combined loading cases. These measurements are normalized by the specimen width.

**Table 4.1 Damage comparisons from solitary thermal loading and combined loading tests.**

Applied heat flux (kW/m <sup>2</sup> )	Front delamination ratio, $d_f/w$		Front charring ratio, $c_f/w$	
	Solitary thermal loading test	Combined loading test	Solitary thermal loading test	Combined loading test
85 kW/m <sup>2</sup>	0.234	0.189	0.203	0.167
140 kW/m <sup>2</sup>	0.281	0.239	0.250	0.216
195 kW/m <sup>2</sup>	0.312	0.267	0.281	0.247

### 4.4.2 Microbuckling Analysis

Figure 4.4 shows the results of the microbuckling damage that occurred during the combined thermal and compressive loading tests. The results of the microbuckling damage ratio of the exposed surface,  $m_f/w$ , versus the applied compressive force were plotted for each test [Figure 4.4]. It can be seen that for a constant thermal load, there is

an increase in microbuckling length with an increase in applied compressive force. Similarly, with a constant compressive force, there is an increase in microbuckling length with an increase in applied thermal load. There also appears to be a critical microbuckling ratio at which value the specimen can no longer sustain the applied compressive load and undergoes global failure through collapse. This phenomenon is shown by the dramatic increase in microbuckling ratio from approximately 0.481 to 1.0 (where microbuckling propagates across the specimen width).

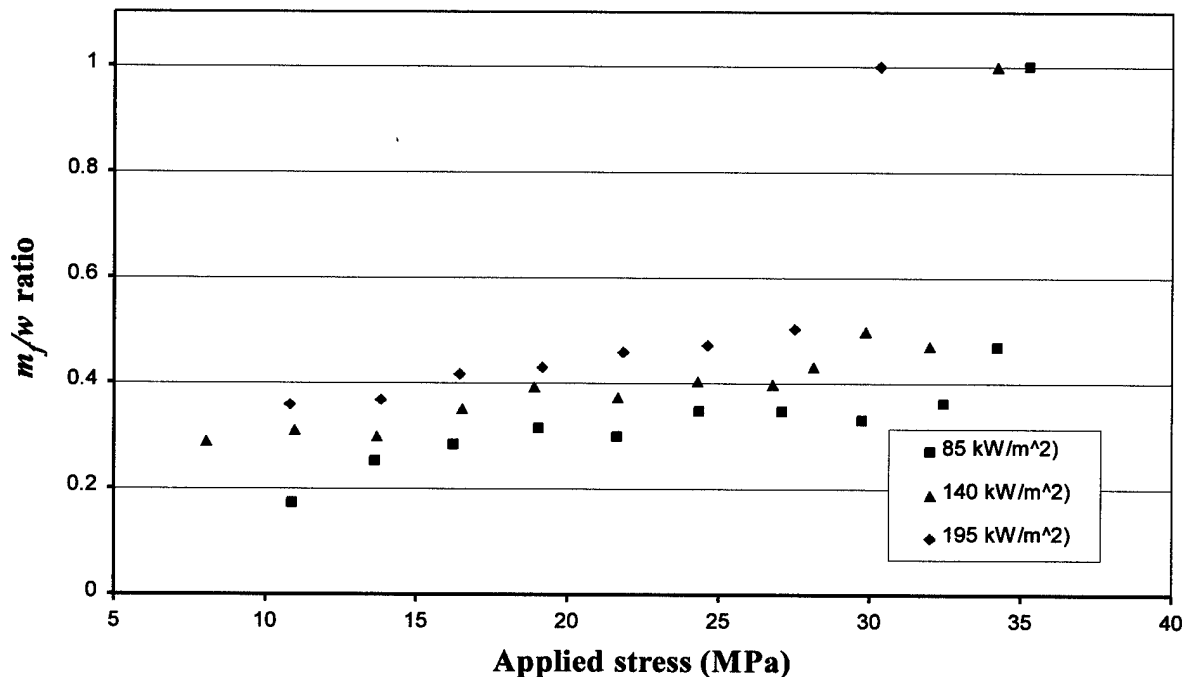


**Figure 4.4 Microbuckling ratio,  $m_f/w$ , versus applied compressive stress for various thermal loading conditions.**

By applying the data from Figure 4.4, a reasonable correlation can be made between the microbuckling strength of the material with respect to position and the microbuckling damage at that position. This correlation was accomplished by

determining the empirical factor  $k$  for the microbuckling strength corresponding to this material. First, the shear modulus curves were adjusted to account for the variation between the temperature profiles of the unexposed surface and the exposed surface. Due to the thermal gradient through the thickness of the material, the temperatures experienced by the unexposed surfaces were less than the temperatures experienced by the exposed surfaces. This variation in temperature and, therefore in modulus, is accounted for by shifting the modulus curves of Figure 4.3 by a factor of 2.54 mm along the distance axis. This adjustment can be verified by the physical differences of the charring radii on the exposed and unexposed surfaces of the specimens for the combined loading tests, which averages to approximately 2.54 mm.

Next, the microbuckling strength curves were then derived through Eq. (4.6) using the adjusted modulus curves of Figure 4.3 and applying an empirical  $k$  factor of 0.03 for each case. These curves were then plotted along with the microbuckling ratio data. The distances of microbuckling and the distance locations correlating to the fiber microbuckling strength values were normalized by the specimen width resulting in a distance ratio,  $x/w$ . This ratio,  $x/w$ , is defined as the distance from the mid point of incident flux normalized by the specimen width. As can be seen in Figures 4.5(a) through Figure 4.5(c), for each distance ratio of microbuckling damage, the applied stress corresponding to that ratio is greater than the fiber microbuckling strength at that position. This shows that the specimen sustained microbuckling damage at positions where the applied load exceeded the degraded microbuckling strength of the material. This observation assumes a uniform stress distribution across the specimen cross-section.

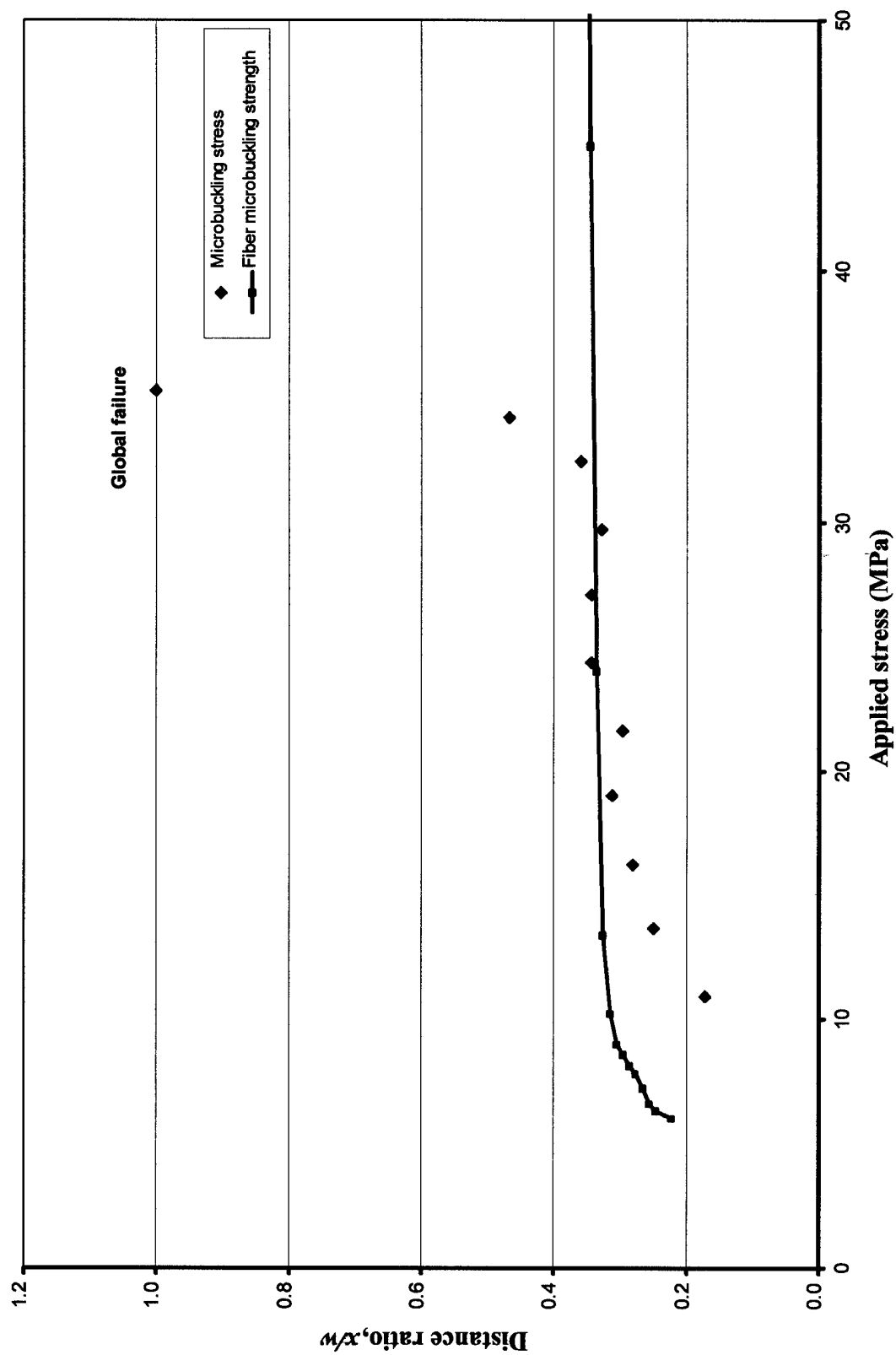
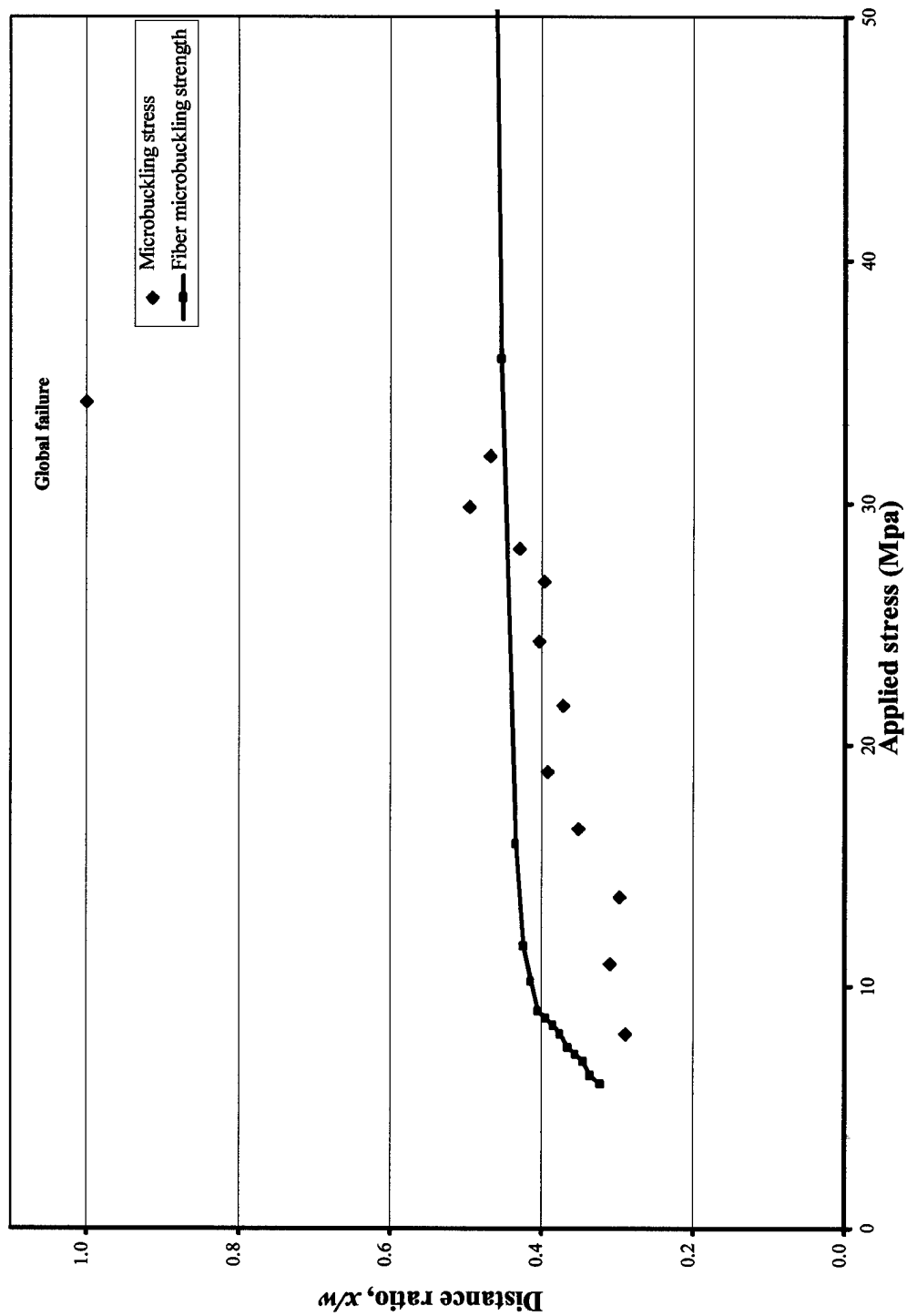


Figure 4.5(a) Microbuckling length as a function of applied compressive stress for a thermal load of 85 kW/m<sup>2</sup>.



**Figure 4.5(b)** Distance ratio of microbuckling as a function of applied compressive stress for a thermal load of 140 kW/m<sup>2</sup>.

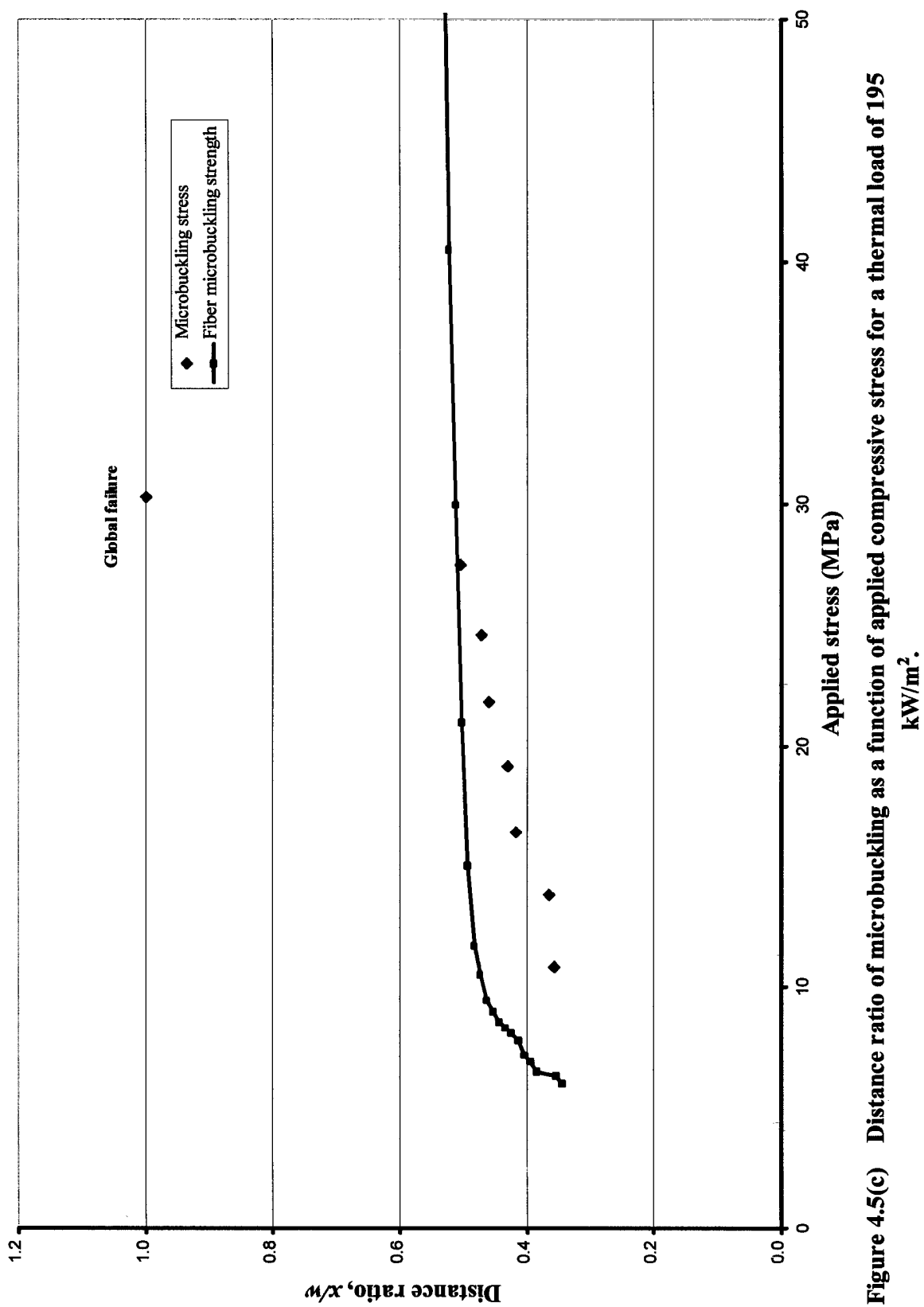


Figure 4.5(c) Distance ratio of microbuckling as a function of applied compressive stress for a thermal load of 195

Where the fiber microbuckling strength increased significantly due to the increase in shear modulus, global failure appeared to dominate the failure mode resulting in catastrophic collapse of the material. In cases of pure compressive loading along the in-plane direction, a plate typically experiences buckling and is able to sustain increased loading until an ultimate load is reached and the load carrying capacity begins to decrease gradually. However, in the case of the combined loading tests, the plates experienced a catastrophic collapse at or near the buckling load. As the intensity of the thermal loading increased, the collapse load decreased, yet, the microbuckling ratio at the initiation of failure was consistent for each thermal loading condition. This consistency suggests that there is a critical microbuckling ratio for the specific material geometry, at which point the specimen can not sustain the applied load if global buckling is initiated and microbuckling propagates through the width of the specimen.

The concept of a stress concentration factor, introduced by the damaged material, may also be an added factor to the initiation of microbuckling. Due to the limitations in time and resources, this theory was not fully investigated. However, a description of the proposed theory and evidence from former research is presented in Appendix C and may provide preliminary direction for further analysis.

#### **4.4.3 Discussion**

From the evaluation of damage, an elementary design criteria can be developed to minimize the effects of local thermal loading on the integrity of a composite structure. It is seen through both the unloaded thermal tests and the combined loading tests that a material exposed to thermal loading will experience damage in the form of delamination and charring. This damage is highly dependent on the thermal loading condition. These

thermal loading conditions can be influenced by certain design measures which influence the heat transfer through the material, such as the type of materials used for fixtures or the use of intumescent coatings which inhibit pyrolysis. However, while the effects of these conditions can be decreased, their existence may be inevitable. Therefore, the safety of the structural design can be better controlled through the optimization of the parameters of structure geometry and applied load.

The specimen geometry is critical in determining the amount of applied compressive stress seen by the structure. It is also critical in determining the heat transfer characteristics of the material. By maximizing the thickness of the structure within the weight and size limitations, the buckling strength and maximum load carrying capacity of the structure will be increased. The rate of dissipation of thermal energy through the material will also be increased, resulting in a decrease in the intensity of the local region of thermal energy concentration and thus a decrease in the damage created. By limiting the applied compressive load on the structure, the possibility of exceeding the degraded fiber microbuckling strength of the material is minimized. This precaution results in the decreased chance of microbuckling and global buckling, therefore decreasing the chance of catastrophic failure in case of thermal loading.

Figure 4.6 shows the quantitative behavior of the damage ratio as a function of applied compressive load. The damage ratio is defined as the length of damage across the structure mid-plane, either through charring, delamination, or microbuckling, normalized by the structure width. As can be seen in the figure, the damage ratio is minimized at a finite value dependent on the intensity of thermal loading. As the applied

compressive load increases, the ratio increases until a critical combination of applied load and damage ratio are reached and the structure collapses.

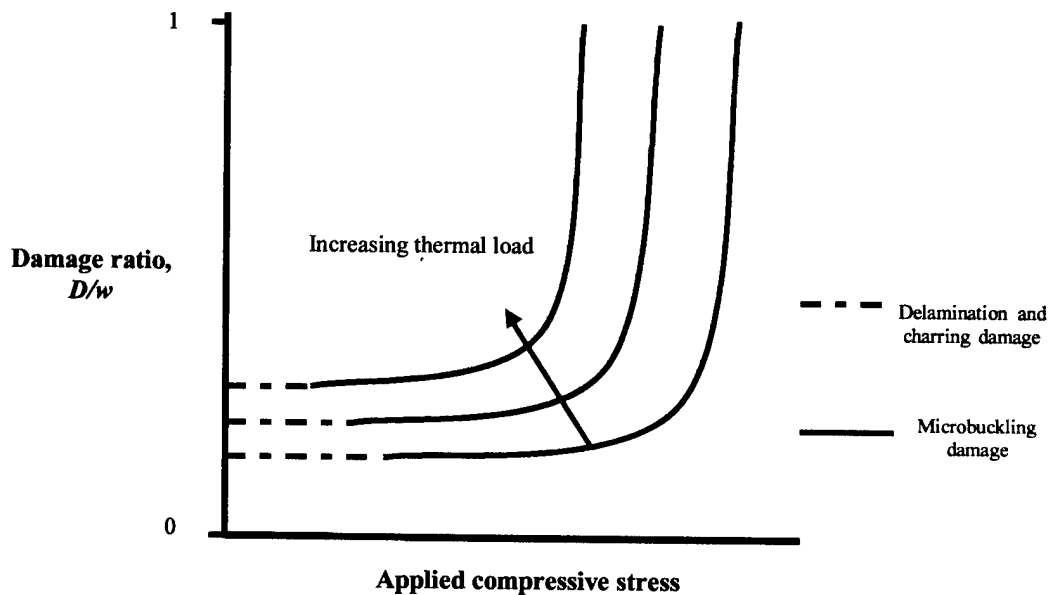


**Figure 4.6** Damage ratio as a function of applied compressive stress

Using the above analysis and the damage evaluation previously discussed, a post-exposure analysis can also be conducted to determine the structural integrity of structures after thermal loading has been applied. If the compressive loading conditions of the structure are known and physical damages can be assessed, the criticality of the damage ratio can be assessed by applying the correlations of Figure 4-H for the specific structure.

As was previously mentioned and can be derived from Figure 4.6, limiting the applied thermal load extends the compressive load carrying capacity of the structure as well. While this may be a difficult factor to control, it must be stated that by decreasing

the applied thermal load, material damage and the degradation of structural properties can be minimized.

## ***Chapter 5 Summary and Conclusions***

The objective of this research was to determine the compressive behavior of composite laminates exposed to local thermal loading. By characterizing the failure modes associated with these combined loading conditions, design criteria may be developed to optimize the mechanical integrity of composite structures subjected to situations involving elevated temperatures. These criteria are particularly critical to the further implementation of composite materials in naval applications, where the resilience of their properties to thermal loading is imperative to the safety of personnel and mission accomplishment.

The material specimens tested were glass/epoxy laminate plates 0.318 cm thick, 10.16 cm wide, and 12.7 cm long. A screw-driven testing machine was used to apply compressive loading and an infrared spot heater was used to apply thermal loading. The duration of each test was five minutes or the onset of catastrophic failure.

Two types of testing were conducted. The first type involved the radiant thermal testing of the material specimens. These tests were conducted to obtain a baseline from which the effects of thermal loading on the physical properties of the composite specimen were determined. For each applied heat flux, the thermal load was concentrated on the center of one side of the specimen. The temperature profile of the back of each specimen for each loading condition was recorded using an infrared imaging camera. At the completion of each test, the material damage was measured and recorded.

The second type conducted was a combined loading test that included thermal and mechanical loading of the specimens. During these tests, the specimens were loaded in

compression to a constant applied load. While subjected to this compressive load, a local thermal load was then applied to the center of the specimen for the duration of the test.

From the thermal tests, the primary physical damage observed was delamination and charring. This damage, measured by the diameter of the area, was shown to increase with an increase in the intensity of thermal loading. In the combined loading tests, delamination and charring were again present, however, microbuckling was the primary form of damage and the dominant failure mechanism. The microbuckling that occurred was dependent upon both the intensity of thermal loading and the amount of applied compressive loading. As the thermal load and the compressive load increased, the length of microbuckling increased. This microbuckling initiated at the center of thermal loading and propagated perpendicular to the direction of compressive loading outward towards the side of the specimen. At or near the global buckling load of the specimen, the microbuckling reached a critical length of approximately one half of the specimen width and the specimen collapsed catastrophically.

An evaluation of the damage measurements found that delamination and charring damage were primarily dependent upon the thermal loading condition while the existence of microbuckling proved variable with the applied compressive load. With this observation, microbuckling was determined to be the critical mechanism for specimen failure and was thus extensively investigated. When compared with the degraded microbuckling strength along the specimen mid-plane, it was seen that where the applied load exceeded the microbuckling strength of the material, microbuckling was initiated. There was also a critical ratio of microbuckling length to specimen width where the dominant failure mechanism of the specimen transitioned from local failure to global

failure. At this ratio, approximately .481, the specimen collapsed catastrophically. The concept of a stress concentrator formed by the degraded region of material was also introduced as an appendix, however, due to limitations in analysis, this concept was not expanded upon.

From the results of the testing and the apparent correlation of microbuckling length to the reduced fiber microbuckling strength, design limitations were developed to minimize the potential effects of local thermal loading. These limitations include optimizing the thickness of the composite structure and minimizing the compressive load applied to the composite structure. By optimizing the structure's thickness, the thermal energy concentration at the local region is decreased, reducing the damage created. An increased thickness also increases the load carrying capacity. Minimizing the applied load felt by the structure decreases the potential for microbuckling initiated by loads in excess of the fiber microbuckling strength. It also reduces the chance for the inception of global buckling and catastrophic failure. A post-exposure evaluation can also be developed from the results presented. If the applied load is known and the damage can be assessed, the damage ratio can be determined and the structural integrity of the laminate can be determined post-thermal exposure.

The research presented in this thesis is only an initial step in the determination and evaluation of the effects of local thermal loading on the integrity of composite structures in compression. It presents the primary phenomena introduced by these loading conditions, however, a more complete analysis is required to completely characterize their behavior and to assist in the prevention of their occurrence. Advanced modeling analysis is necessary to determine the stress distributions introduced by thermal

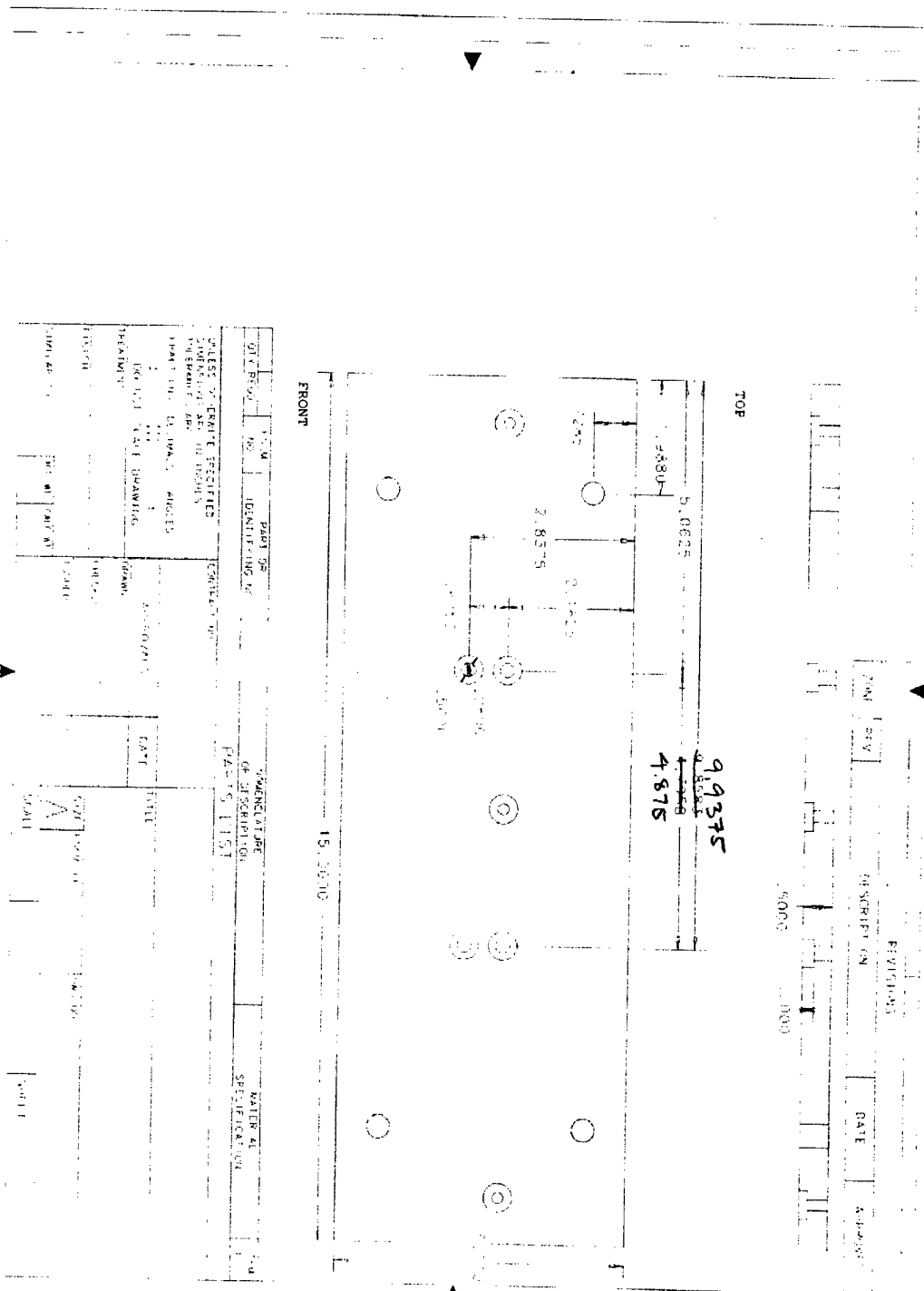
expansion and material property degradation. The concept of a stress concentrator formed by the region of degraded material should also be investigated.

## References

1. Mouring, S., 1998, "Composites for Naval Surface Ships," *MTS Journal*, Vol. 32, No.2, pp.41-46.
2. "Sea Duty for Composites," *Advanced Materials and Processes*, Vol. 14, No. 2, Aug. 1992, pp.16-20.
3. Hepburn, R.D. LCDR, USN, Magliulo, G., and Wright, T., 1991, "The U.S. Navy's New Coastal Minehunter (MHC): Design, Material, and Construction Facilities," *Naval Engineers Journal*, May, pp 60-73.
4. Blank, D.A., Bock, A.E., and Richardson, D.J., 1985, "*Introduction to Naval Engineering*," Naval Institute Press, Annapolis, MD.
5. Asaro, R.J., and Dao, M., 1997, "Fire Degradation of Fiber Composites," *Marine Technology*, Vol. 34, No. 3, July, pp.197-210.
6. Milke, J.A., and Vizzini, A.J., 1991, "Thermal Response of Fire-Exposed Composites," *Journal of Composites Technology & Research*, Vol. 13, No. 3, Fall, pp.145-151.
7. Chang, C. I., 1986, "Thermal Effects on Polymer Composite Structures," *Theoretical and Applied Fracture Mechanics*, Vol. 6, pp.113-120.
8. Asaro, R.J., and Dao, M., 1998, "A Study on Failure Prediction and Design Criteria for Fiber Composites under Fire Degradation," *Composites: Part A*, Vol. 30, pp.123-131.
9. Anderson, T.L., 1995, "*Fracture Mechanics: Fundamentals and Applications*," CRC Press, New York.
10. Barbero, E.J., 1999, "*Introduction to Composite Materials Design*," Taylor and Francis, Inc., Philadelphia.
11. Griffis, C.A., Nemes, F.R., Stonesifer, F.R., and Chang, C.I., 1986, "Degradation in Strength of Laminated Composites Subjected to Intense Heating and Mechanical Loading," *Journal of Composite Materials*, Vol. 20, May, pp. 216-235.
15. "Instron Model 5583 Load Frame Operator's Guide", M10-25583-1, June 1993, Issue A.
16. Material Safety Data Sheet, <http://MSDS.PDC.CORNELL.EDU/msds/siri/q424/q111.html>.
17. Jones, R.M., 1975, *Mechanics of Composite Materials*, Taylor and Francis, Washington, D.C.
18. Rosen, B.W., 1965, "Mechanics of Composite Strengthening," *Fiber Composite Materials*, American Society for Metals, Metals Park, OH.
19. Gibson, R.F., 1994, "*Principles of Composite Material Mechanics*," McGraw-Hill, Inc., New York.
20. Buckley, C.P., Bucknall, C.B., and McCrum, N.G., 1997, "*Principles of Polymer Engineering*," Oxford University Press, Oxford.

21. Kroschwitz, J.I., executive editor, 1990, "*Concise Encyclopedia of Polymer Science and Engineering*," John Wiley & Sons, Inc., New York.
22. Micarta products brochure.
23. Discussion with International Paper technical representative, manufacturer of Micarta G10 FR4.
24. Swancor, Inc., <http://www.swancor.com.tw/brominated.html>
25. Waddoups, M.E., Eisenmann, J.R., and Kaminski, B.E., 1971, *Journal of Composite Materials*, Vol. 5, pp. 446-454.
26. Whiteside, J.B., Daniel, I.M., and Rowlands, R.E., 1973, "The Behavior of Advanced Filamentary Composite Plates with Cutouts," Air Force Flight Dynamics Laboratory Technical Report AAFDDL-TR-73-48, June.
27. Nuismer, R.J. and Whitney, J.M., 1975, "Uniaxial Failure of Composite Laminates Containing Stress Concentrations," *Fracture Mechanics of Composites, ASTM STP 593*, American Society for Testing Materials, pp.117-142.
28. Nuismer, R.J. and Whitney, J.M., 1974, "Stress Fracture Criteria for Laminated Composites Containing Stress Concentrations," *Journal of Composite Materials*, Vol. 8, p.253.
29. Nuismer, R.J., and Labor, J.D., "Applications of the Average Stress Failure Criterion: Part II – Compression," *Journal of Composite Materials*, Vol. 13, January, p.49.
30. Lekhnitskii, S.G., 1968, *Anisotropic Plates*, translated from the Second Russian Edition by S.W. Tsai and T. Cheron, Gordon and Breach, Science Publishers, Inc., New York.
31. Ashton, J.E., and Whitney, J.M., 1970, *Theory of Laminated Plates*, Technomic Publishing Co., Stamford, Conn.
32. Khamseh, A.R., and Waas, A.M., 1992, "Failure Mechanisms of Uni-ply Composite Plates with a Circular Hole Under Static Compressive Loading," *Journal of Engineering Materials and Technology*, Vol. 114, pp.304-310.

### Figure A.1 Base Plate Fixture



[illegible]

**FRONT**

**TOP**

1.5000  
.5000  
2.5000  
.3750  
.5625  
1.1250  
5.0000  
1.2500  
1.375  
9.000  
5.000  
1.0000  
5.000

UNLESS OTHERWISE SPECIFIED  
DIMENSIONS ARE IN INCHES  
FRACTIONS DECIMALS ANGLES  
XX  
ON NET SCALE DRAWING  
TOLERANCE  
FINISH  
STANDARD TO  
NOT TO SCALE

DESIGN NO.  
PART OR IDENTIFYING NO.  
QUANTITY NO.  
APPROVALS  
DATE  
SHEET

REVISIONS  
DATE  
APPENDIX

## Appendix B Theoretical Euler Buckling Analysis

Buckling equation:

$$P_{CR} = \frac{\pi^2 EI}{(KL)^2}$$

where

$$I = \frac{1}{12}bh^3$$

$P_{CR}$  = critical buckling load

$E$  = elastic modulus

$I$  = moment of inertia

$b$  = width

$h$  = thickness

$L$  = length

$K$  = end factor

Specimen dimensions and properties:

$E = 20.7 \text{ GPA}$

$b = 10.2 \text{ cm}$

$h = .318 \text{ cm}$

$L = 10.2 \text{ cm}$

$K = .75$

Calculations:

$$I = \frac{1}{12}(10.2\text{cm})(.318\text{cm})^3 = .0273\text{cm}^4 = 2.73 \times 10^{-10} \text{ m}^4$$

$$P_{cr} = \frac{\pi^2 \left( 20.7 \times 10^9 \frac{\text{N}}{\text{m}^2} \right) (2.73 \times 10^{-10} \text{ m}^4)}{(.75 \times .102\text{m})^2} = 9530 \text{ N}$$

# Appendix C Specimen Damage Measurements

Table C.1 Specimen Damage Measurements

Heat Setting	Specimen	Applied stress (Pa)	Front delamination ratio, $d_f/w$	Front charring ratio, $c_f/w$	Front microbuckling ratio, $m_f/w$	Rear delamination ratio, $d_r/w$	Rear charring ratio, $c_r/w$	Rear microbuckling ratio, $m_r/w$
85 kWm <sup>2</sup>	.125-4-5-50	1.09E+07	0.188	0.172	0.172	0.188	0.110	
	.125-4-5-51	1.36E+07	0.188	0.165	0.251	0.267	0.110	
	.125-4-5-52	1.62E+07	0.172	0.157	0.282	0.188	0.125	
	.125-4-5-53	1.90E+07	0.188	0.172	0.313	0.188	0.125	0.313
	.125-4-5-54	2.16E+07	0.188	0.172	0.298	0.282	0.125	0.298
	.125-4-5-55	2.44E+07	0.188	0.173	0.345	0.188	0.126	0.298
	.125-4-5-56	2.71E+07	0.189	0.157	0.346	0.267	0.126	0.315
	.125-4-5-57	2.97E+07	0.188	0.173	0.329	0.173	0.125	0.298
	.125-4-5-58	3.24E+07	0.188	0.173	0.361	0.188	0.125	0.314
	.125-4-5-59	3.42E+07	0.188	0.156	0.469	0.203	0.125	0.281
	.125-4-5-60	3.53E+07	.156**	0.141**	1.000	.141**	.078**	1
	140 kW/m <sup>2</sup>	.125-4-5-29	8.04E+06	0.228	0.209	0.288	0.228	0.156
.125-4-5-30		1.09E+07	0.237	0.212	0.309	0.232	0.150	0.257
.125-4-5-31		1.37E+07	0.222	0.206	0.297	0.225	0.145	0.288
.125-4-5-32		1.65E+07	0.235	0.214	0.350	0.222	0.149	0.306
.125-4-5-41		1.89E+07	0.232	0.209	0.394	0.278	0.172	0.349
.125-4-5-43		2.17E+07	0.254	0.227	0.373	0.245	0.137	0.306
.125-4-5-44		2.43E+07	0.242	0.217	0.405	0.227	0.162	0.380
.125-4-5-45		2.68E+07	0.247	0.227	0.398	0.247	0.157	0.402
.125-4-5-47		2.81E+07	0.252	0.220	0.431	0.246	0.156	0.361
.125-4-5-46		2.98E+07	0.253	0.227	0.499	0.245	0.161	0.356
.125-4-5-61		3.20E+07	0.222	0.204	0.471	0.218	0.134	0.351
.125-4-5-49		3.42E+07	0.158**	0.128**	1.000	0.132**	0.074**	1.000
195 kW/m <sup>2</sup>	.125-4-5-64	1.10E+07	0.283	0.242	0.358	0.261	0.202	
	.125-4-5-65	1.38E+07	0.285	0.253	0.369	0.268	0.202	0.323
	.125-4-5-66	1.66E+07	0.270	0.248	0.418	0.241	0.200	0.330
	.125-4-5-67	1.93E+07	0.260	0.248	0.430	0.258	0.212	0.383
	.125-4-5-68	2.21E+07	0.254	0.244	0.459	0.264	0.207	0.387
	.125-4-5-69	2.48E+07	0.260	0.250	0.473	0.255	0.205	0.413
	.125-4-5-70	2.76E+07	0.257	0.242	0.504	0.274	0.197	0.424
	.125-4-5-71	3.03E+07	0.281**	0.250	1.000	.266**	.188**	1.000

## Appendix D Stress Concentration Analysis

### Background

As established in the Chapter 3, there is a significant decrease in the shear modulus of the composite with the application of a thermal load. This area of degradation creates not only a local weakness, as in the case of microbuckling, but possibly a global weakness as well. The circular pattern of degradation on the surface penetrates through the thickness, which may simulate the existence of a notch or cutout in the specimen. The intensity and duration of thermal loading could determine the size of this “notch”. Like a notch, this volume of thermally degraded material compromises the strength of the specimen and, with the application of a uniaxial compressive load, creates a stress concentration in the material. The following section discusses the analysis of a notch in a laminate plate, previous research characterizing failure due to a notch, and the correlation to the findings of this current research.

Application of the classical stress concentration factor (SCF) analysis can not be used in the case of laminated plates containing a circular cutout with diameters less than one inch. This has been proven through experimental data for specimens in tension [25,26]. Nuismer and Whitney [27,28,29] developed failure criteria for predicting the uniaxial tensile and compressive strength which accounted for this hole size factor. Their analysis is based on the normal stress distribution that exists ahead of the hole and the greater ability for smaller sized holes to redistribute higher stresses.

Their analysis first considered a hole of radius  $R$  in an infinite orthotropic plate. Assuming the application of a uniform stress  $\bar{\sigma}$  parallel to the y-axis, the normal stress,  $\sigma_y$ , along the x-axis in front of the hole can be predicted by

$$\sigma_y(x,0) = \frac{\bar{\sigma}}{2} \left\{ 2 + \left( \frac{R}{x} \right)^2 + 3 \left( \frac{R}{x} \right)^4 - (K_T^\infty - 3) \left[ 5 \left( \frac{R}{x} \right)^6 - 7 \left( \frac{R}{x} \right)^8 \right] \right\} \quad (C.1)$$

where  $K_T^\infty$  is the orthotropic stress concentration factor for an infinite width plate [30]. It is defined as follows

$$K_T^\infty = 1 + \sqrt{\frac{2}{A_{22}} \left( \sqrt{A_{11}A_{22}} - A_{12} + \frac{A_{11}A_{22} - A_{12}^2}{2A_{66}} \right)} \quad (C.2)$$

where  $A_{ij}$  are the in-plane laminate stiffnesses determined from laminated plate theory

[31]. By plotting the ratio  $\frac{\sigma_y}{\bar{\sigma}}$  with respect to the distance ahead of the hole (X-R),

Figure D.1 shows that although two different sized holes have the same stress concentration factor at the edge of the hole, the stress concentration is much more localized for the smaller hole.

When Eq. (D.1) is plotted as a function of (X-R), the normal stress  $\sigma_y$  in front of

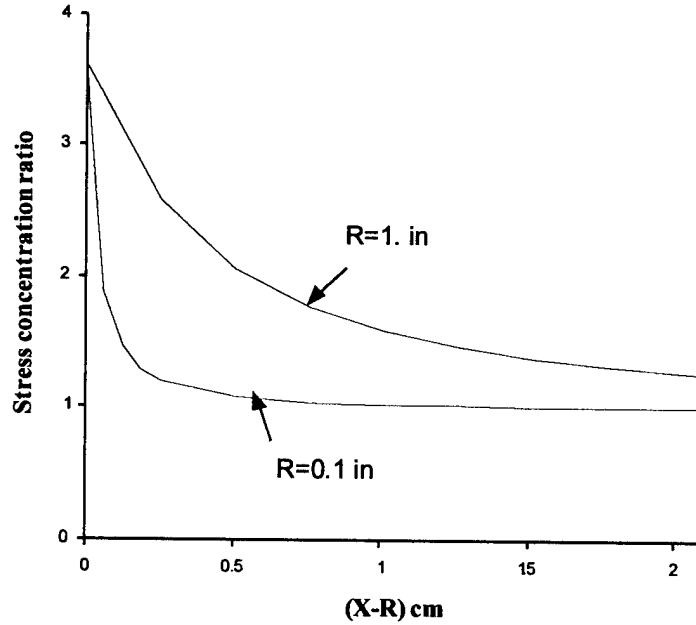


**Figure D.1** Stress concentration ratio as a function of distance ahead of the hole for a circular hole in an infinite isotropic plate

the hole, along the midplane, can be determined for a given hole size. In Figure D.2, the normal stress is plotted for an applied load of 33.1 MPa. As can be seen the load experienced by the plate at the hole edge is almost four times greater than the applied load.

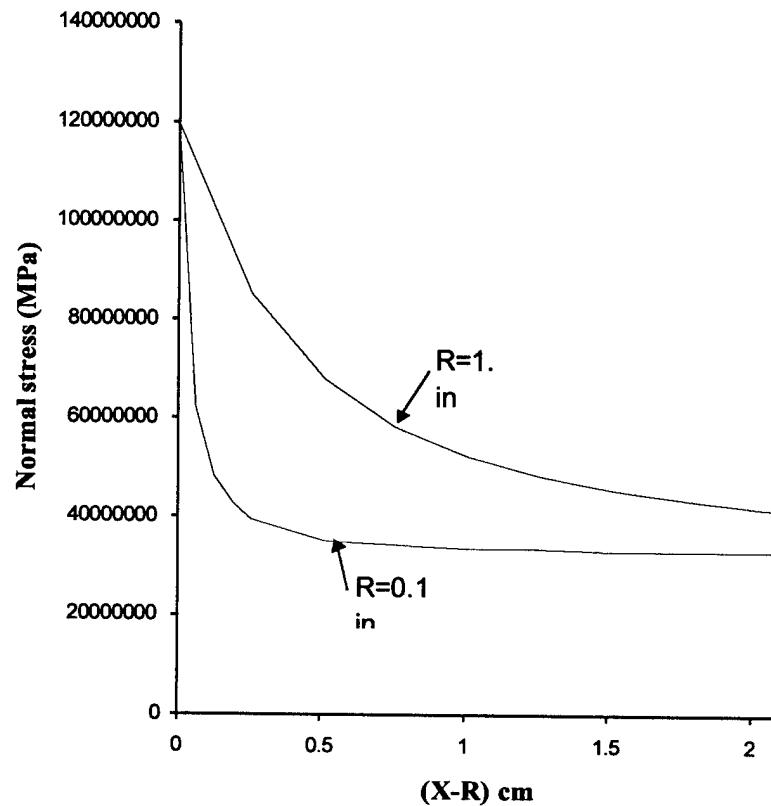


**Figure D.2 Normal stress as a function of distance ahead of the hole for a circular hole in an infinite isotropic plate**

In summary, the presence of a notch in a laminate plate creates an increased normal stress that is perpendicular to the applied load and exists along the x-axis in front of the notch. This stress distribution is dependent upon the hole size and increases with an increase in hole size. Furthermore, it can be derived, that while the applied load imposed upon the laminate plate may be below the compressive and microbuckling

strength of the laminate, the normal stress along the x-axis may exceed those strengths significantly resulting in fiber microbuckling and collapse of the laminate.

Investigations conducted by Khamseh and Wass [32] support this analysis. Their research was concerned with the effects of notches on the compressive behavior of laminate plates and characterized the effects of the hole diameter on the compressive strength and failure mode of the laminate plate. The material tested was a low modulus, high strength, unidirectional graphite/epoxy laminate. During the tests, the specimens were loaded in uniaxial compression. Specimens of different hole sizes were tested, some of which were loaded to global failure and others of which were only loaded to the inception of localized failure.

The results found that the predominant failure mode for the laminate was determined to be by fiber microbuckling/kinking at the hole edge followed by delamination near the failure site, resulting in the propagation of damage into the interior of the specimen. It was also determined that fiber microbuckling preceded delamination failure and that the initiation of fiber microbuckling was dictated by the hole size. If the ratio of the cutout diameter to the specimen width ( $d/w$ ) was greater than .062, then fiber microbuckling was initiated at the hole edge. If the ratio  $d/w$  was smaller than .062, then failure occurred at the specimen edge and in most cases, the specimen failed due to global buckling.

This failure behavior is similar to that experienced by test specimens subjected to combined thermal and mechanical loading. Like the specimens containing a cutout, the specimens subjected to combined loading conditions experienced the initiation of microbuckling at the center of the specimen, where thermal loading was concentrated.

This microbuckling also propagated perpendicular to the applied load outward to the edges. The length of microbuckling was dependent upon the applied load, which would be magnified considerably at the x-axis in the presence of a notch resulting in a larger area of stress distribution. As discussed in Chapter 3, there is a significant decrease in the shear modulus of the material at elevated temperatures. As was discussed, this reduction in shear modulus results in a decrease in the fiber microbuckling strength of the material leading to microbuckling. However, this reduction in shear modulus may also result in a stress concentration in the specimen that could create an even greater stress distribution.

Due to time limitations, preliminary analyses were done, however, a thorough modeling analysis was not conducted to determine the applicability of this theory. It is suggested that this area be further researched as another factor in determining the compressive response of composite materials to local thermal loading.

## Appendix E DMA Analysis

Rheometrics Rhios V4.3.2

WED 04 JAN 80  
Fri 04-Jan-80 - 7:53:18am

EXPERIMENT: MICARTA G10 Rheometric Temp. Scan

Page 1

TEST TYPE: Dynamic Temperature Ramp  
DATE/TIME: Fri 04-Jan-80 - 9:14:04am  
FILENAME: B:\VOL001\MICARTA.DAT  
INSTRUMENT: RDS-7700 s/n 1604  
OPERATOR: RAS

### TEST CONDITIONS:

Geometry Type ..... Torsion Rectangular (Tors Rect)  
Length ..... 45.25 [mm]  
Width ..... 12.76 [mm]  
Thickness ..... 2.37 [mm]  
Frequency ..... 10.0 [rad/s]  
Initial Temp. .... 40.0 [°C]

### EXPERIMENT SCALARS:

FREQ..... 10.000 [rad/s]  
DENSITY..... 0.0000 [gm/cm3]  
TOOL\_EXPAN..... 0.0000 [µm/°C]

### EXPERIMENT NOTES:

EXPERIMENT: MICARTA G10 Rheometric Temp. Scan

Page 2

### TEST PARAMETERS:

Save Geometry As .....  
Geometry Type ..... Torsion Rectangular (Tors Rect)  
Length ..... 45.25 [mm]  
Width ..... 12.76 [mm]  
Thickness ..... 2.37 [mm]  
Test Type ..... Dynamic Temperature Ramp (DTempRamp)  
Save Setup As .....  
Frequency ..... 10.0 [rad/s]  
Initial Temp. .... 40.0 [°C]  
Final Temp. .... 300.0, 0.0, 0.0, 0.0, 0.0, 0.0, 0.0, 0.0 [°C]  
Ramp Rate ..... 5.0, 0.0, 0.0, 0.0, 0.0, 0.0, 0.0, 0.0 [°C/min.]  
Zone Time ..... 2:00:00, 0, 0, 0, 0, 0, 0, 0 [s or h:m:s]  
Time Per Measure ..... 30, 0, 0, 0, 0, 0, 0, 0 [s or h:m:s]  
Strain ..... 0.025, 0.0, 0.0, 0.0, 0.0, 0.0, 0.0, 0.0 [%]  
Options .....  
Delay Before Test ..... Off  
Delay Before Test ..... 0 [s or h:m:s]  
AutoStrain ..... Off  
Max Applied Strain ..... 0.0 [%]  
Max Allowed Torque ..... 0.0 [gm·cm]  
Min Allowed Torque ..... 0.0 [gm·cm]  
Strain Adjustment ..... 0.0 [% of Current Strain]  
Measurement Options .... Manual Delay Settings  
Cycles ..... 0.0 []  
Correlation: One Cycle Correlate On  
Turn OFF Motor ..... No  
Turn Hpld ON ..... No  
Turn OFF Temp Controller No  
Set End of Test Temp ... No  
END TEST PARAMETERS

EXPERIMENT: MICARTA G10 Rheometric Temp. Scan

Page 1

No.	G' dyn/cm <sup>2</sup>	G'' dyn/cm <sup>2</sup>	G* dyn/cm <sup>2</sup>	tan_delta .....	Temp °C	time s
1	7.4413e+10	1.2632e+09	7.3271e+10	0.0170	38.984	6.0000
2	7.3022e+10	1.2251e+09	7.2842e+10	0.0168	39.594	36.000
3	7.2445e+10	1.1784e+09	7.2585e+10	0.0163	42.813	66.000
4	7.2160e+10	1.1352e+09	7.2207e+10	0.0157	45.148	96.000
5	7.1812e+10	1.1013e+09	7.1820e+10	0.0153	47.914	126.00
6	7.1370e+10	1.0670e+09	7.1348e+10	0.0149	50.035	156.00
7	7.0949e+10	1.0198e+09	7.0943e+10	0.0144	52.613	186.00
8	7.0585e+10	9.6260e+08	7.0601e+10	0.0136	55.090	216.00
9	7.0225e+10	9.1140e+08	7.0243e+10	0.0130	57.438	246.00
10	6.9827e+10	8.7857e+08	6.9823e+10	0.0126	60.027	276.00
11	6.9405e+10	8.6666e+08	6.9478e+10	0.0125	62.418	306.00
12	6.8995e+10	8.7362e+08	6.8933e+10	0.0127	64.969	336.00
13	6.8620e+10	8.9317e+08	6.8555e+10	0.0130	67.445	366.00
14	6.8266e+10	9.0677e+08	6.8406e+10	0.0133	70.082	396.00
15	6.7880e+10	8.9011e+08	6.7826e+10	0.0131	72.473	426.00
16	6.7385e+10	8.4639e+08	6.7476e+10	0.0126	74.848	456.00
17	6.6765e+10	8.1974e+08	6.6896e+10	0.0123	77.527	486.00
18	6.6117e+10	8.5869e+08	6.6049e+10	0.0130	79.813	516.00
19	6.5580e+10	9.7422e+08	6.5388e+10	0.0148	82.391	546.00
20	6.5196e+10	1.1144e+09	6.5159e+10	0.0171	84.941	576.00
21	6.4870e+10	1.1921e+09	6.5117e+10	0.0184	87.355	606.00
22	6.4465e+10	1.1881e+09	6.4406e+10	0.0184	89.855	636.00
23	6.3931e+10	1.1713e+09	6.4030e+10	0.0183	92.172	666.00
24	6.3320e+10	1.1989e+09	6.3291e+10	0.0189	94.934	696.00
25	6.2716e+10	1.2631e+09	6.2762e+10	0.0201	97.586	726.00
26	6.2157e+10	1.3234e+09	6.2092e+10	0.0213	99.789	756.00
27	6.1619e+10	1.3712e+09	6.1628e+10	0.0223	102.23	786.00
28	6.1044e+10	1.4453e+09	6.1213e+10	0.0237	104.64	816.00
29	6.0371e+10	1.5859e+09	6.0386e+10	0.0263	107.07	846.00
30	5.9556e+10	1.7997e+09	5.9609e+10	0.0302	109.57	876.00
31	5.8576e+10	2.0683e+09	5.8800e+10	0.0353	111.90	906.00
32	5.7399e+10	2.3894e+09	5.7513e+10	0.0416	114.43	936.00
33	5.5916e+10	2.8089e+09	5.6116e+10	0.0502	116.82	966.00
34	5.3850e+10	3.4135e+09	5.4418e+10	0.0634	118.98	996.00
35	5.0734e+10	4.2861e+09	5.1648e+10	0.0845	121.73	1026.0
36	4.6088e+10	5.4223e+09	4.7463e+10	0.1177	124.10	1056.0
37	3.9803e+10	6.6186e+09	4.1328e+10	0.1663	126.85	1086.0
38	3.2414e+10	7.4577e+09	3.4257e+10	0.2301	129.07	1116.0
39	2.4925e+10	7.5413e+09	2.6704e+10	0.3026	131.54	1146.0
40	1.8306e+10	6.7985e+09	1.9670e+10	0.3714	134.08	1176.0
41	1.3100e+10	5.5156e+09	1.4391e+10	0.4210	136.30	1206.0
42	9.3768e+09	4.1020e+09	1.0187e+10	0.4375	138.90	1236.0
43	6.9071e+09	2.8639e+09	7.3301e+09	0.4146	141.42	1266.0
44	5.3582e+09	1.9264e+09	5.5392e+09	0.3595	143.85	1296.0
45	4.4216e+09	1.2781e+09	4.5021e+09	0.2891	146.27	1326.0
46	3.8613e+09	8.5225e+08	3.8955e+09	0.2207	148.67	1356.0
47	3.5172e+09	5.7953e+08	3.5322e+09	0.1648	151.28	1386.0
48	3.2936e+09	4.0678e+08	3.2847e+09	0.1235	154.30	1416.0
49	3.1418e+09	2.9788e+08	3.1525e+09	0.0948	156.22	1446.0
50	3.0377e+09	2.2983e+08	3.0303e+09	0.0757	158.90	1476.0
51	2.9639e+09	1.8792e+08	2.9518e+09	0.0634	161.18	1506.0
52	2.9058e+09	1.6184e+08	2.9243e+09	0.0557	163.91	1536.0
53	2.8562e+09	1.4376e+08	2.8597e+09	0.0503	166.45	1566.0

54	2.8157e+09	1.2874e+08	2.7995e+09	0.0457	168.67	1596.0
55	2.7852e+09	1.1556e+08	2.7900e+09	0.0415	171.23	1626.0
56	2.7597e+09	1.0526e+08	2.7645e+09	0.0381	173.43	1656.0
57	2.7315e+09	9.8013e+07	2.7404e+09	0.0359	176.14	1686.0
58	2.6986e+09	9.2081e+07	2.7014e+09	0.0341	178.99	1716.0
59	2.6661e+09	8.5830e+07	2.6570e+09	0.0322	181.60	1746.0
60	2.6387e+09	8.0164e+07	2.6365e+09	0.0304	183.60	1776.0
61	2.6133e+09	7.7592e+07	2.6299e+09	0.0297	186.07	1806.0
62	2.5828e+09	7.8873e+07	2.5762e+09	0.0305	188.48	1836.0
63	2.5441e+09	8.0825e+07	2.5566e+09	0.0318	191.05	1866.0
64	2.5016e+09	7.8070e+07	2.5001e+09	0.0312	193.46	1896.0
65	2.4611e+09	6.9314e+07	2.4530e+09	0.0282	195.95	1926.0
66	2.4235e+09	5.9353e+07	2.4355e+09	0.0245	197.79	1956.0
67	2.3837e+09	5.2823e+07	2.3740e+09	0.0221	200.57	1986.0
68	2.3372e+09	5.0308e+07	2.3622e+09	0.0215	203.52	2016.0
69	2.2849e+09	4.9742e+07	2.2705e+09	0.0217	207.43	2046.0
70	2.2331e+09	4.9282e+07	2.2385e+09	0.0220	207.25	2076.0
71	2.1872e+09	4.9239e+07	2.1796e+09	0.0225	210.54	2106.0
72	2.1477e+09	5.1054e+07	2.1539e+09	0.0238	212.95	2136.0
73	2.1117e+09	5.4909e+07	2.1056e+09	0.0260	215.40	2166.0
74	2.0780e+09	5.9050e+07	2.0831e+09	0.0284	217.81	2196.0
75	2.0484e+09	6.1739e+07	2.0445e+09	0.0301	219.73	2226.0
76	2.0225e+09	6.3420e+07	2.0245e+09	0.0314	222.59	2256.0
77	1.9925e+09	6.5491e+07	1.9904e+09	0.0329	225.04	2286.0
78	1.9472e+09	6.7704e+07	1.9768e+09	0.0348	228.18	2316.0

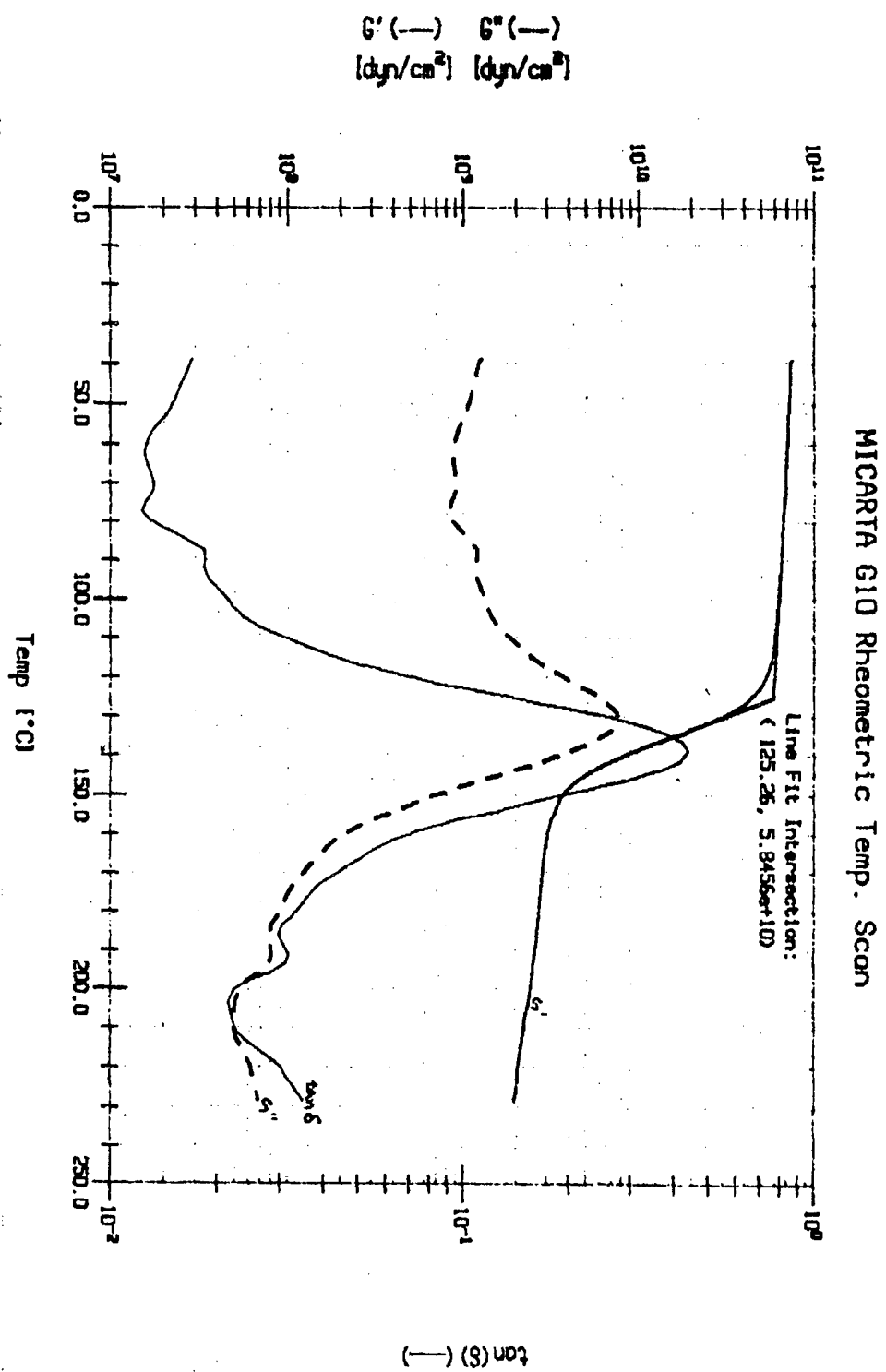


Figure E.1 Micarta G10 Rheometric Temperature Scan